An incoherent broadband cavity-enhanced absorption spectrometer for simultaneous NO_3 and N_2O_5 measurements, integrated into a NO_y instrument suite: characterization and first field deployment

Patrick Dewald[1], Sergio Harb[2], Bénédicte Picquet-Varrault[1], Mathieu Cazaunau[1], Maxime Feingesicht[1], Lucas Beltran[1], Vincent Michoud[3], Xavier Landsheere[1], Edouard Pangui[1], Antonin Bergé[1], Christopher Cantrell[1], and Manuela Cirtog[1]

[1] Université Paris Est Créteil and Université de Paris Cité, CNRS, LISA, F-94010 Créteil, France
[2] Institut National de l'Environnement industriel et des Risques (INERIS), F-60550 Verneuil en Halatte, France
[3] Université Paris Cité and Université Paris Est Créteil, CNRS, LISA, F-75013 Paris, France

Correspondence to: Patrick Dewald (patrick.dewald@lisa.ipsl.fr), Manuela Cirtog (manuela.cirtog@lisa.ipsl.fr)

Abstract. Reactive nitrogen species (NO_y) are involved in the formation of secondary pollutants, thus following their interconversions is crucial for understanding their impact on air quality. While nitric oxide (NO) and nitrogen dioxide (NO_2), are important contributors to total NO_y, further constituents such as the nitrate radical (NO_3) and dinitrogen pentoxide (N_2O_5), formed from NO_2 oxidation, are key intermediates in nocturnal oxidation processes. Even though NO_3 and N_2O_5 affect the NO_y budget in the following day, their role is poorly constrained in isolated measurements. We present the "NOyBOx", a new instrumental framework combining measurements of NO, NO_2 and NO_y from commercial analyzers with a custom-built incoherent broadband cavity-enhanced absorption spectrometer (IBBCEAS) that measures NO_3 directly and N_2O_5 via a thermal dissociation inlet (TDI) and channel differencing. We describe the design of the IBB-CEAS subsystem, characterize the TDI, cavity optics, transmission losses, and, using a synthetic spectra simulation approach, the bias of ambient NO_2 and water vapor on our concentration retrieval procedure. Under optimal laboratory conditions we find a limit of detection (LOD) of 1.5 and 2.2 pptv (1σ Allan deviation, 15 s) for NO_3 and N_2O_5, respectively. Under field conditions, interference by water vapor and NO_2 worsens these LODs to 3.1 pptv with a total measurement uncertainty (TMU) of 12% for NO_3, and to 4.4 pptv with a mean TMU of 21% for N_2O_5. Exemplary results from its first deployment during a field campaign in a temperate forest atop a 40 m tall tower are discussed.

1 Introduction

Reactive nitrogen species, collectively referred to as NO_y, constitute a broad class of atmospheric trace gases involved in the formation of secondary pollutants such as tropospheric ozone (O_3) and particulate matter (Crutzen and Lelieveld, 2001; Kiendler-Scharr et al., 2016), as well as in the regulation of the atmosphere's oxidative capacity (Geyer et al., 2001a; Monks, 2005). Consequently, NO_y species play a crucial role in air quality, human health and climate (Lelieveld et al., 2020; Wild et al., 2016). Even though natural sources of NO_y emissions exist, NO_y is predominantly released into the atmosphere in the form

of nitric oxide (NO) through combustion processes, that is readily converted to nitrogen dioxide (NO_2) in the presence of typical ambient O_3 levels (Dutta et al., 2026; Logan, 1983). At the same time, NO_2 is partially photolysed to NO by sunlight during the day. This interconversion between NO and NO_2 is reflected in the use of the term NO_x, which denotes the sum of these two species (Seinfeld and Pandis, 2012). While NO_x can often form the dominant fraction of NO_y in freshly polluted air masses (Pandey Deolal et al., 2012), it is progressively oxidized to a diverse suite of further (often secondary) reactive nitrogen species ($NO_z = NO_y – NO_x$) including nitric acid (HNO_3), nitrous acid (HONO), organic nitrates ($RONO_2$ and RO_2NO_2) in both gas and particle phase (pNO_3), the nitrate radical (NO_3), dinitrogen pentoxide (N_2O_5), halogenated nitrogen species (e.g. nitryl chloride, $ClNO_2$), and others (Finlayson-Pitts and Pitts, 2000). As air masses undergo chemical processing, the contribution of NO_z to the NO_y budget often increases with air mass age (Brown et al., 2017; Parrish et al., 1993; Stratmann et al., 2016). Several NO_z species, notably HNO_3 and organic nitrates, are sufficiently long-lived to be transported over long distances and later re-release NO_x in remote regions, thereby effectively functioning as NO_x reservoirs and further impacting air quality (Ito et al., 2007; Lee et al., 2016; Pye et al., 2015, 2010; Rindelaub et al., 2015).

One particularly important species among reactive nitrogen compounds crucially impacting the formation potential of particulate matter is the above-mentioned NO_3 radical: It is formed from oxidation of NO_2 by O_3 (R1) and is in thermal equilibrium with NO_2 and N_2O_5 (R2 and R3) (Wayne et al., 1991). Since NO_3 is readily photolysed by sunlight (R4a and R4b) or rapidly reacts with NO (R5), its mixing ratios remain too low to be detected during the day (Brown and Stutz, 2012).

$$NO_2 + O_3 \rightarrow NO_3 + O_2 \quad \text{(R1)}$$

$$NO_3 + NO_2 + M \rightarrow N_2O_5 + M \quad \text{(R2)}$$

$$N_2O_5 + M \rightarrow NO_3 + NO_2 + M \quad \text{(R3)}$$

$$NO_3 + h\nu \rightarrow NO_2 + O\,(^3P) \quad \text{(R4a)}$$

$$NO_3 + h\nu \rightarrow NO + O_2 \quad \text{(R4b)}$$

$$NO_3 + NO \rightarrow 2NO_2 \quad \text{(R5)}$$

$$NO_3 + \text{VOC} \rightarrow \text{products (e.g. } HNO_3\text{, SOA, organic nitrates)} \quad \text{(R6)}$$

$$N_2O_5 + \text{surface (e.g. particles)} \rightarrow \text{products} \quad \text{(R7)}$$

During the night, in the absence of sunlight and at low NO levels, NO_3 has been shown to be an important oxidant for unsaturated biogenic volatile organic compounds (BVOC) such as isoprene and terpenes (Brown and Stutz, 2012; Dewald et al., 2024; Hu et al., 2023; Liebmann et al., 2019; Mermet et al., 2021; Mogensen et al., 2015; Ng et al., 2017). In urban environments, anthropogenic volatile organic compounds (AVOC), especially phenolic compounds, are also efficiently oxidized by NO_3 (Bolzacchini et al., 2001; Zhang et al., 2025). These reactions between BVOC or AVOC and NO_3 (R6) can yield high amounts of the NO_x reservoir species detailed above including organic nitrates, nitric acid and secondary organic aerosol, all of which can significantly impact air quality, climate, and human health (Fry et al., 2014; Kumar et al., 2023; Ng et al., 2017; Schueneman et al., 2025; Wennberg et al., 2018). In addition, N_2O_5 (and therefore indirectly NO_3) can be irreversibly removed through heterogeneous hydrolysis on e.g. aerosols (R7), producing nitrate that can be ultimately lost by

wet or dry deposition (Aldener et al., 2006; Brown et al., 2009; Phillips et al., 2016). These processes can be an important sink for NO_x, with NO_3 and N_2O_5 acting as the key intermediates linking nocturnal chemistry to the removal of NO_y and, consequently, to reduced ozone formation on the following day (Finlayson-Pitts and Pitts, 2000; Kane et al., 2001).

The NO_3 radical is highly reactive, so its nocturnal mixing ratios rarely exceed a few parts per trillion by volume (pptv), especially in forests (Liebmann et al., 2018; Mermet et al., 2021; Yáñez-Serrano et al., 2018), and it shows strong spatio-temporal variability (Brown et al., 2007; Vrekoussis et al., 2007). Detecting it therefore requires techniques with both high sensitivity and fast time resolution.

Platt et al. (1980) made the first tropospheric NO_3 measurements using differential optical absorption spectroscopy (DOAS), which determines a gas' concentration by measuring how much light of specific wavelengths it absorbs along a long open-air light path (often several km) between a light source and a distant detector. Because of its exceptional sensitivity at that time, long-path DOAS became one of the most widely used NO_3 methods (Geyer et al., 2001b; McLaren et al., 2004; Platt et al., 1981; Sommariva et al., 2007). However, it only yields a concentration averaged over the whole absorption path, giving it poor spatial resolution, and it cannot operate under snow or fog (Platt and Stutz, 2008).

Since then, several alternative techniques have emerged: laser-induced fluorescence (LIF) (Matsumoto et al., 2005; Wood et al., 2003), cavity ring-down spectroscopy (CRDS) as well as cavity-enhanced absorption spectroscopy (CEAS) (Berden et al., 2000; Brown, 2003; Brown and Stutz, 2012; Lin et al., 2026). Both CRDS and CEAS work by trapping light inside an optical cavity formed by two highly reflective mirrors, so that light is reflected thousands of times before escaping. This effectively folds a path of many kilometers into a compact cell, greatly amplifying the light's interaction with trace gases without requiring a long open-air path.

CRDS has become a particularly powerful tool for measuring atmospheric trace gases, including NO_3, thanks to its spatial resolution, sensitivity, and accuracy (Ball et al., 2001; Bitter et al., 2005; Dubé et al., 2006; Li et al., 2018; Lin et al., 2022; Odame-Ankrah and Osthoff, 2011; Schuster et al., 2009; Sobanski et al., 2016; Türk et al., 2026; Wagner et al., 2011; Wang et al., 2015; Wu et al., 2020). Rather than measuring absorbed light directly as in DOAS, CRDS infers concentration from how quickly light intensity decays ("rings down") inside the cavity once a pulse (pulsed CRDS) or continuous source (cw-CRDS) is switched off: gases in the cavity absorb light and shorten this decay time, and the change in decay rate gives the concentration. Operating at a narrow wavelength range, CRDS suffers only negligible interference from O_3, H_2O, or NO_2, achieves effective path lengths of tens of kilometers, and reaches, as recently reviewed in Türk et al. (2026), detection limits often below 1 pptv for a few seconds of averaging. It also requires less power and is smaller and lighter than DOAS setups.

Incoherent broadband cavity-enhanced absorption spectroscopy (IBBCEAS), first proposed by Fiedler et al. (2003) is a variant of these cavity techniques that has gained increasing popularity as a means of detecting NO_3 in field and chamber measurements (Ball et al., 2004; Dorn et al., 2013; Fouqueau et al., 2020; Kennedy et al., 2011; Langridge et al., 2008; Ling et al., 2023; Nam et al., 2022; Suhail et al., 2019; Varma et al., 2009; Venables et al., 2006; Ventrillard-Courtillot et al., 2010; Wang et al., 2017, 2023; Wang and Lu, 2019). Unlike CRDS, which uses a single laser wavelength and needs fast-response detectors to track the decay, IBBCEAS setups consist of simpler and lower-cost components by coupling a broadband (multi-

wavelength) light source into the cavity and measuring the resulting absorption spectrum, thereby avoiding the need for fast detection electronics while keeping much of the cavity-enhanced sensitivity. This gives IBBCEAS advantages of both DOAS and CRDS: like DOAS, its broadband source allows simultaneous measurement of multiple trace gases (Ling et al., 2023; Nam et al., 2022), rather than the single-species selectivity of CRDS; like CRDS, its compact optical path makes it easy to combine with other in-situ data for analyzing local atmospheric chemistry and physics. Both CEAS and CRDS are also flexible enough to deploy on ground stations, towers, vehicles, ships, and aircrafts to capture spatio-temporal variations in NO_3 at local scales, and, unlike DOAS, both are largely unaffected by weather conditions.

Finally, quantifying ambient N_2O_5 indirectly requires thermally dissociating it into NO_3 before detection by any of the techniques mentioned above (Dubé et al., 2006; Sobanski et al., 2016; Türk et al., 2026; Wang et al., 2017). Alternatively, a thermal dissociation inlet can be coupled to a chemical-ionization mass spectrometer , allowing N_2O_5 to be detected indirectly through the formation and subsequent detection of e.g. NO_3^- (Kercher et al., 2009; Slusher et al., 2004).

As detailed in Fuchs et al. (2010), NO_x is commonly measured using optical methods including DOAS, CRDS, CEAS, laser-induced fluorescence (LIF), cavity attenuated phase shift (CAPS) and chemiluminescence detection (CLD). The latter quantifies NO with detection limits in the pptv range based on the detection of chemiluminescent emission of excited NO_2 formed from the reaction of NO with excess O_3 (Clough and Thrush, 1967; Hosaynali Beygi et al., 2011; Tadic et al., 2020). To quantify NO_2, it is first converted to NO, typically by photolysis or catalytic conversion prior to entering the detection cell (Nussbaumer et al., 2021; Reed et al., 2016). A LIF-based NO_2 measurement relies on excitation of NO_2 at wavelengths above 400 nm and fluorescence detection above 600 nm (Day et al., 2002; Javed et al., 2019). DOAS detects ambient NO_2 by exploiting its structured absorption spectrum between 400 and 600 nm, using either broadband light sources over long optical paths or natural sunlight (Leser et al., 2003; Merten et al., 2011). Cavity techniques such as CRDS, CAPS and CEAS rely on NO_2 visible absorption but enhance sensitivity through long effective optical path lengths achieving excellent detection limits below 50 pptv (Fuchs et al., 2010; Gherman et al., 2008; Sobanski et al., 2016; Thieser et al., 2016; Wild et al., 2014). In case of CAPS, NO_2 concentrations are deduced from the phase shift of the modulated light transmitted through the cavity, which is directly related to the optical attenuation caused by the presence of NO_2 (Ge et al., 2013; Kebabian et al., 2005). NO can likewise be quantified through these techniques by first converting it to NO_2 via oxidation with O_3 (Friedrich et al., 2020; Ohara et al., 2024; Wüst et al., 2025).

Early NO_y measurements relied on converting reactive nitrogen species to NO using heated gold or molybdenum converters, followed by chemiluminescence detection (CLD). Gold converters were designed to exclude particulate nitrate, whereas molybdenum converters also responded to particulate nitrate (Fahey et al., 1986; Williams et al., 1998). More recently, thermal dissociation techniques have been adopted, in which NO_z species are thermally decomposed to NO_2 prior to detection by LIF or cavity-enhanced absorption methods (Day et al., 2002; Dewald et al., 2026a; Paul et al., 2009; Wild et al., 2014). Although these approaches provide high sensitivity and speciation capability, elevated temperatures can induce secondary reactions that generate measurement artefacts. These effects can be mitigated by operating at reduced pressure or scavenging reactive

radicals, although additional corrections based on laboratory calibration and chemical modelling may still be required (Womack et al., 2017; Wüst et al., 2025).

Here, we present the NOyBOx, an integrated instrument suite that simultaneously measures NO_3, N_2O_5, NO, NO_2, and NO_y. As outlined in the chemical framework above, NO_3 and N_2O_5 can not only influence NO_x-NO_y partitioning but also remove reactive nitrogen from the atmosphere via heterogeneous loss of N_2O_5, NO_3, and its oxidation products (e.g. organic nitrates, HNO_3). Previous multi-channel instruments have combined NO_3/N_2O_5 measurements with measurements of selected additional nitrogen species, such as organic nitrates and NO_2 (Kennedy et al., 2011; Sobanski et al., 2016), or measured total NO_y without speciated NO_3/N_2O_5 measurements (Friedrich et al., 2020; Wild et al., 2014). One exception is a six-channel CRDS instrument as detailed in Brown et al. (2017), which included channels for O_3, N_2O_5, NO, NO_2, and total NO_y, as well as NO_3, although NO_3 measurements were not successfully obtained during that deployment. NOyBOx combines two custom optical cavities for NO_3/N_2O_5 measurements with commercial analyzers for NO_x species and total NO_y. This configuration provides the combined measurements needed to investigate the role of nocturnal oxidation processes in the reactive nitrogen budget that remains barely accessible with isolated measurements, while potentially reducing instrument complexity and cost compared with an approach based entirely on custom CRDS channels. In the following sections we describe the instrument's design, characterize its NO_3/N_2O_5 subsystem and present results from its first field deployment during the Atmospheric ChemistRy Of the Suburban foreSt (ACROSS) campaign.

2 Instrument design and methodology

As depicted in Fig. 1, the NOyBOx instrument consists of three commercial analyzers for the measurement of NO, NO_2, and NO_y (blue-shaded), two custom-built IBBCEAS cavities for the quantification of ambient NO_3 and N_2O_5 (grey-shaded), installed in a portable rack (120 x 80 x 150 cm), and a gas supply assembly (orange-shaded) for zeroing and calibration of both subsystems. The instrument can be operated in three modes: (i) ambient sampling, (ii) background measurements by supplying both subsystems with zero air (ZA) from a synthetic air cylinder (purity ≥ 99.9999 %, Air Liquide, Alphagaz), and (iii) calibration using a standard gas containing a known NO_2 concentration (800 parts per billion by volume (ppbv) in N_2/O_2, Air Liquide). During ambient sampling, air is drawn through three dedicated inlets (Fig. 1, purple): inlet 1 supplies the NO_3 IBBCEAS cavity, inlet 2 supplies the N_2O_5 IBBCEAS cavity, and inlet 3 supplies the commercial analyzers. The NO_3 and N_2O_5 IBBCEAS inlets are equipped with a polytetrafluoroethylene (PTFE) membrane filter (Pall Corporation, R2PJ047) in a PTFE holder (Mace, 930-1244-101) to remove particles with a diameter bigger than 2 µm that would worsen the detection limit through scattering and deposition on mirror surfaces when entering the instrument. The commercial analyzers are equipped with internal filters. During background and calibration, gas flows are regulated by critical orifices (CrO). The mode switching in the commercial analyzer subsystem and the N_2O_5 channel is enabled by 3/2-way solenoid valves consisting of PTFE (Bürkert, type 0121, no. 20063588), while a 2-way solenoid PTFE valve (Bürkert, type 0121, no. 77191) in combination with a Perfluoroalkoxy alkane (PFA) T-piece (Swagelok, PFA-420-3) is used in the NO_3 channel for reasons of hardware

availability. Excess gas in the latter is vented via its own sampling inlet, whereas a dedicated overflow outlet (OFL) is used for the former. In both cases, the corresponding vents are equipped with removable charcoal cartridges to prevent the release of calibration gases into the ambient air. A technical scheme detailing the exact gas flows and positions of the components is available in the Supplement (Fig. S1). Operation of the instrument is fully automated through a custom Python software, which controls the mass flow controllers (MFCs), the heaters, and the valve switching between operating modes. It also executes ambient measurements, background, and calibration sequences, and continuously acquires data from the optical cavities, gas analyzers, and auxiliary sensors (temperature, pressure). Details of the individual instrument components are provided in the following subsections.

2.1 Commercial analyzer subsystem for NO_2, NO and NO_y

Our measurements of NO, NO_2 and NO_y rely on commercial analyzers that have already been thoroughly tested in the past and are widely used by the geoscience community. Their description below is thus limited on a purely technical level and do not require any further characterization. During field operation, they are zeroed with synthetic air using the background mode. Each analyzer is generally calibrated against another commercial CLD (Horiba, APNA-370) by injecting well-defined amounts of NO and/or NO_2 (typically 2–100 ppbv) into the Multiphase Atmospheric Experimental Simulation Chamber (CESAM) prior to field deployment (Wang et al., 2011). Alternatively, the analyzers were calibrated by direct injection of well-defined NO and NO_2 standards using a dilution system, with NO_2 additionally calibrated by gas-phase titration of excess NO with O_3.

2.1.1 NO_2 analyzer

A CAPS instrument (TELEDYNE API, Model T500U) measures NO_2 via absorption of radiation from a light emitting diode (LED, 450 nm center wavelength) inside a cavity equipped with two highly-reflective mirrors and a vacuum photodiode detector. The cavity is thermostated (45 °C) to prevent water condensation on the mirror surfaces and minimize temperature-induced variations in the NO_2 absorption cross section. It features a low zero drift (< 0.1 ppbv d^{-1}) and provides a limit of detection (LOD) of 40 pptv (30 s) with a relative precision of 0.5 %. The analyzer samples with ca. 0.9 standard (STP) litres per minute (SLPM).

2.1.2 NO analyzer

NO was measured using a chemiluminescence-based NO analyzer (ECO PHYSICS CLD 780 TR). Excess O_3 required for NO detection (see above) is supplied by an integrated ozone generator operated under low pressure (ca. 14 mbar) maintained by an external vacuum pump.

The instrument's limit of detection is 10 pptv (1 min), with a sample flow rate of 3 SLPM. The ozone generator can be fed with either pure O_2 or dry ambient air (0.3 SLPM); both configurations were used during the ACROSS campaign (section 4). When operating on ambient air, we dried the supply air using a silica gel cartridge that was periodically renewed. Note that maximum sensitivity and accuracy was achieved when supplying the ozone generator with pure O_2.

2.1.3 NO_y analyzer

NO_y are transformed to NO by a gold converter (ECO PHYSICS CON 765) and detected by a second ECO-PHYSICS CLD 780 TR analyzer. This converter operates by reducing all NO_y species through a reaction with CO catalyzed on a gold surface at high temperature (300 °C). The sample flow is set to 3 SLPM and the CO flow is 0.03 SLPM. The NO analyzer was first calibrated alone, with the gold converter disconnected, either using the CESAM chamber or direct injections (see above). The converter was then reconnected and its conversion efficiency determined by generating a known NO_2 concentration and comparing the resulting NO_x signal to that of the Horiba APNA-370 analyzer, yielding a conversion efficiency of 88%.

2.2 IBBCEAS subsystem for NO_3 and N_2O_5

The two IBBCEAS channels (Fig.1, grey-shaded) exploit the extended optical path length achievable within a high-finesse optical cavity in order to attain a sufficiently high sensitivity to detect NO_3 and N_2O_5 at ambient concentration levels. Both channels target the strongest absorption band of the NO_3 channel at 662 nm (Orphal et al., 2003). To enable detection of N_2O_5, the sample air is first passed through a 1 m Perfluoroalkoxy alkane (PFA) thermal dissociation inlet (TDI) operated at 80–200°C (residence times of 0.12 – 0.16 s), which quantitatively dissociates N_2O_5 into NO_3 and NO_2 (R3). The resulting stream then enters the N_2O_5 cavity, maintained at 80°C to suppress the reverse recombination reaction (R2). The signal in this channel reflects the sum of ambient NO_3 and N_2O_5, from which N_2O_5 is isolated by difference with the NO_3 channel (see below). Although this cavity technically detects the sum of two components, for simplicity we refer to it as the N_2O_5 channel throughout the text. Gas flows through both cavities (7 SLPM for NO_3 and 5 SLPM for N_2O_5 resulting in residence times of 1.31 s and 1.53 s, respectively) are regulated by dedicated mass flow controllers (Alicat, MCP-20SLPM) and operated at a fairly stable intracavity pressure (970 mbar, typical value at ground level), before being combined, pumped through a charcoal trap, and vented. All connections and lines upstream the cavity consist of PFA to ensure reduced NO_3 losses.

2.2.1 Light source

In each channel, light is provided by a thermally stabilized red LED (NO_3: Mouser Electronics – Starboard, Luminus SST-10-DR-B130 Deep Red, max. 430 mW; N_2O_5: Thorlabs M660D2) with a near-Gaussian emission profile centered at 657.4 nm (FWHM 18 nm) and 660.4 nm (FWHM 21 nm) for the NO_3 (Fig. 2a, blue line) and N_2O_5 channels, respectively. Precise thermal regulation to ± 0.01 °C (as specified by the manufacturer) via a thermoelectric cooler (Arroyo Instruments, Laser Mount) driven by a laser diode controller (Arroyo Instruments, model 6310), at operating currents of 650 mA and 1150 mA for the NO_3 and N_2O_5 channels, suppresses wavelength drift and intensity instabilities that would otherwise corrupt the spectral baseline. The different operating currents originate from deploying two different types of LEDs. Under these operating conditions, we observed no statistically relevant long-term drifts in the centre wavelength with values (± 2σ) of (7.3 ± 7.6) pm h^{-1} (NO_3) and (4.7 ± 3.4) pm h^{-1} (N_2O_5), which are below the spectrometer's resolution (> 140 pm, see below). The divergent

LED emission is collimated and focused to the cavity midpoint by an aspheric condenser lens (Thorlabs ACL2520U, 25.0 mm diameter, f = 20 mm, NA = 0.79), ensuring efficient coupling into the cavity.

2.2.2 Cavity

The core of the instrument is a pair of high-finesse optical cavities, each formed by two high-reflectivity mirrors (Layertec, planar/concave, radius of curvature 1 m, diameter 25 mm, nominal reflectivity (99.98 ± 0.01) % at 630–690 nm) separated by 61.5 cm. At this reflectivity, light undergoes thousands of round trips before exiting, accumulating an extended effective path length that is the origin of the technique's sensitivity. The cavity body is a stainless-steel tube (internal diameter 18.5 mm) coated with PFA and sealed with O-rings at each mirror mount. Since any loss of mirror reflectivity directly degrades measurement sensitivity – as made explicit by Eq. (1) below – each mirror is continuously purged with clean and dry zero air (100 sccm, Fig. 1 orange lines) from the gas cylinder (purity ≥ 99.9999 %), delivered through three 1/16-inch (inner diameter) PFA tubing regulated by critical orifices at an upstream pressure of 1.5 bar, preventing aerosol deposition or condensation of semi-volatile compounds on the mirror surfaces.

2.2.3 Detection

The light transmitted through the cavity carries the spectral imprint of the intracavity absorbers. It is collected by a fiber-coupled collimator (Thorlabs, F810-SMA, f = 35.41 mm, NA = 0.25), guided via an optical fiber (Ocean Optics Vis–NIR, 200 µm slit, 1.5 m) to a dedicated spectrometer (Ocean Optics, QE65000) with a CCD thermoelectrically cooled to −15 °C to minimize dark current, and covering 617–724 nm (107 nm bandwidth) and 639–685 nm (46 nm bandwidth) for the NO_3 and N_2O_5 channels, respectively.

2.2.4 Spectral fitting and calculation of ambient mixing ratios

The wavelength-dependent (λ) absorption coefficient of the intracavity sample, $\alpha(\lambda)$, is then retrieved from the ratio of the transmitted intensities measured in the absence (I_0, Fig. 2a, blue) and presence (I, Fig. 2a, black) of the absorbing species (Engeln et al., 1998):

$$\alpha(\lambda) = \left(\frac{1-T(\lambda)}{T(\lambda)}\right)\left(\frac{1-R(\lambda)}{d_{eff}}\right) \quad (1)$$

where $T(\lambda) = I(\lambda)/I_0(\lambda)$ (Fig. 2a, grey dashed), $R(\lambda)$ is the mirror reflectivity, and d_{eff} is the effective mirror distance. Equation (1) makes explicit that $I_0(\lambda)$ and $R(\lambda)$ must be characterized regularly, which is why each is determined, as mentioned above, through a dedicated operating mode: The reference spectrum $I_0(\lambda)$ is recorded in background mode using zero air. The mirror reflectivity $R(\lambda)$ is determined in calibration mode by introducing a known concentration of NO_2 from the standard (800 ppbv) into the cells (see section 3.2).

With $I_0(\lambda)$ and $R(\lambda)$ established, $\alpha(\lambda)$ is fully constrained during ambient sampling (Fig. 2b, black), and the concentrations of individual absorbers are retrieved by fitting their known absorption cross-sections using a least-squares (differential evolution)

algorithm (Storn and Price, 1997) implemented in a custom Python data processing routine including SciPy (Virtanen et al., 2020):

$$\alpha(\lambda) = \sum N_i \sigma_i(\lambda) + p(\lambda) \quad (2)$$

where $\sigma_i(\lambda)$ (cm^2 molecule^{-1}) and N_i (molecule cm^{-3}) are the absorption cross-section and concentration of species i, and $p(\lambda)$ is a cubic polynomial baseline correction accounting for residual source intensity fluctuations (Venables et al., 2006) and particle extinction within the cell (Varma et al., 2013).

Within the spectral range used to monitor NO_3, absorption features from NO_2, H_2O and O_3 are also present. However, given their atmospheric abundances and cross-section magnitudes (Keller-Rudek et al., 2013), all of these contribute meaningfully to the retrieved absorption. In order to quantify NO_3 accurately, the interference by H_2O and NO_2 must be accounted for by including their absorption cross-sections in the fitting routine. The strictly monotonic behaviour of the O_3 absorption spectrum in the considered spectral region allows its contribution to be accounted for within the polynomial baseline correction $p(\lambda)$.

The NO_3 and NO_2 reference cross-sections used in the spectral fitting are taken from Orphal et al. (2003), with a peak value of $(2.13 \pm 0.06) \times 10^{-17}$ cm^2 molecule^{-1} at 298 K and 662.05 nm (Fig. 2c, blue), and Vandaele et al. (1998), respectively (Fig. 2c, orange). Both reference spectra were convolved with the instrument spectral response function.

Since NO_3 absorption cross-sections are temperature-dependent (IUPAC, 2026), a correction was applied when fitting spectra from the heated N_2O_5 cavity (353 K): the convolved cross-section from Orphal et al. (2003) was scaled by the ratio of the 662 nm band peak intensity at 298 K and 353 K following Osthoff et al. (2007), yielding a value of $(1.70 \pm 0.10) \times 10^{-17}$ cm^{2}molecule^{-1} at 353 K. For NO_2, the ambient-temperature reference spectrum (Vandaele et al., 1998) was scaled using the ratio of the cross-sections between 640–650 nm at 298 K and 353 K as reported by Davidson et al. (1988).

Water vapor presents a particular challenge, as its absorption bands partly overlap with those of NO_2 and NO_3, and the relative intensities of its rotational lines vary with ambient humidity and temperature (Aliwell and Jones, 1996), precluding the use of a single synthetic reference spectrum. To circumvent this, we use H_2O reference spectra measured in-situ in the absence of NO_3/N_2O_5 (e.g. clean daytime ambient air, laboratory air or humidified synthetic air from a chamber, Fig. 2c, grey). Since such a reference is an empirical spectrum rather than a literature cross section, it is expressed as an absorption coefficient α as derived from Eq. (1). The H_2O reference in Fig. 2c was obtained by sampling laboratory air shortly before the experiment with its humidity (33% RH at 23 °C) taken from a laboratory hygrometer reading (C2AI, Comet T7318) at the time of recording. The H_2O amount in a sample spectrum is then retrieved from the fitted scaling factor of this reference; for example, the 31.8% RH in Fig. 2b is the scaling factor multiplied by the reference RH. This approach is quantitative only if the reference is recorded shortly beforehand under conditions (in particular temperature) similar to those of the sample. Under such conditions, the retrieved RH agrees well with the CESAM chamber hygrometer (Vaisala HMP234), as suggested by a linear regression analysis yielding a slope (±2σ) close to unity (1.01 ± 0.09, Fig. S2). While CEAS principally allows simultaneous retrieval of multiple species in the general case (Nam et al., 2022), accurate quantification of NO_2 and H_2O can be impeded by potential residual NO_2 in the reference or variability in H_2O relative band intensities in our approach, especially when reference and sample conditions differ. As discussed below with a synthetic spectra analysis (see section 3.5), for accurate NO_3

quantification, what matters is that the NO_2 and H_2O absorption structures are represented in the fit, not the accuracy of the retrieved NO_2 amount: While NO_2 quantification is strongly biased in the presence of water, the NO_3 retrieval accuracy is only marginally impacted. An example fit along with the retrieved concentrations is shown in Fig. 2b (blue line) for a mixture $NO_3/NO_2/H_2O$ generated in CESAM simulation chamber (https://www.cesam.cnrs.fr/). Note that in this example fit, constraining NO_2 to the CAPS measurement (17.9 ppbv) would alter the retrieved NO_3 amount by less than 0.5%. To improve fit accuracy, spectral points near the characteristic absorption features of NO_3 (662 nm), NO_2 (642 nm), and H_2O (651.5 nm) were weighted more heavily via a Gaussian boost function centered on each species' band. In this routine, NO_3 is the target species; NO_2 and H_2O are fitted mainly to account for their spectral interference, and their retrieved amounts are subject to larger uncertainty. Following the example of commonly used fitting routines such as DOASIS (Kraus, 2006), spectral shift and squeeze were treated as free fit parameters (shift bounded to ± 0.1 nm, squeeze to ±1%), rather than fixed values, leading to very low fit residuals (Fig. 2d).

After the purely spectral concentration retrieval, final correction accounts for the loss of NO_3 on surfaces along the sampling path as thoroughly discussed in earlier publications (Fuchs et al., 2008; Türk et al., 2026). In our NO_3 channel, the fitted concentration ($N_{\mathrm{NO_3}}$) must be corrected for the transmission efficiency through the filter (T_{Filter}) and cavity ($T_{\mathrm{NO_3\ channel}}$) according to Eq. 3:

$$[NO_3] = \frac{N_{\mathrm{NO_3}}}{T_{\mathrm{Filter}} \cdot T_{\mathrm{NO_3\ channel}}} \quad (3)$$

Since NO_3 transmission is not necessarily identical across the two channels, deriving N_2O_5 by channel differencing requires a slightly more general expression similar to that derived by Türk et al. (2026):

$$[N_2O_5] = \frac{N_{\mathrm{NO_3+N_2O_5}} - T_{\mathrm{Filter}} \cdot T_{\mathrm{N_2O_5\ channel}} \cdot [NO_3]}{T^*_{\mathrm{N_2O_5\ channel}}}, \quad (4)$$

with the fitted NO_3 concentration in the N_2O_5 channel $N_{\mathrm{NO_3+N_2O_5}}$, the corrected NO_3 concentration [NO_3] calculated from Eq. 3, and the transmission efficiencies through filter and the combined transmission of TDI and N_2O_5 cavity ($T_{\mathrm{N_2O_5\ channel}}$). Note that NO_3 resulting from N_2O_5 dissociation only resides in the cavity, therefore a slightly higher transmission has to be applied ($T^*_{\mathrm{N_2O_5\ channel}}$, Türk et al., 2026). As discussed below, heterogeneous N_2O_5 losses within the instrument are not considered. Cavity temperature and pressure, monitored at the outflow of each cavity, are used to convert all retrieved concentrations from molecule cm^{-3} to mixing ratios. When the NO_3 cavity temperature strongly differs from ambient temperature, NO_3 levels must be corrected to account for the shift in the highly temperature-dependent NO_2-NO_3-N_2O_5 equilibrium (reactions R2 and R3) during the residence time in the cavity.

3 Characterization of the IBBCEAS subsystem

The retrieval of NO_3 and N_2O_5 concentrations from IBBCEAS measurements requires accurate determination of the cavity absorption coefficient as described in Sect. 2. According to Eq. (1), the absorption coefficient depends on the effective cavity

length (d_{eff}) and the mirror reflectivity (R). The effective cavity length accounts for the reduction of the geometric cavity length caused by the mirror purge flows and is therefore required to determine the true optical path within the cavity. Once d_{eff} has been established, R can be determined, enabling calculation of the wavelength-dependent cavity absorption coefficient and, consequently, quantitative retrieval of NO_3 and N_2O_5 concentrations through the spectral fitting procedure according to Eq. (2).

Additional instrument characterizations are required to account for the thermal conversion and sampling efficiencies as shown in Eqs. (3–4) of the measurement system: Since N_2O_5 is quantified via thermal dissociation to NO_3, a thermogram is recorded to determine the temperature at which maximum conversion is achieved, ensuring quantitative conversion while avoiding unnecessary heating. Furthermore, transmission losses throughout the sampling and optical path are characterized to determine the fraction of NO_3 reaching the cavity. These characterization steps require to sample stable amounts of NO_3 (and N_2O_5) through the NO_3/N_2O_5 subsystem. To achieve this, we mixed 10-50 standard (STP) cubic centimetre per minute (sccm) of NO_2 from the calibration bottle (800 ppbv) with O_3 in a Teflon-coated (FEPD-121, Chemours) 0.4 L glass reactor. Ozone was generated by 185 nm photolysis of O_2 in a 60 sccm flow of dry zero air. The resulting ca. 70–110 sccm reactant flow leads to a residence time of ca. 5 min and was diluted in 5 SLPM and 7 SLPM dry synthetic air prior to sampling through the NO_3 and N_2O_5 channel, respectively. In this configuration, $NO_3 + N_2O_5$ mixing ratios of 0.05–1 ppbv were attained.

3.1 The effective cavity length

As indicated above, the presence of a zero air purge flow (100 sccm) to prevent the deposition of particles on the mirror surfaces reduces the geometric cavity path length of 61.5 cm to an effective cavity length d_{eff}. To estimate it we coupled the NO_3 source to the cavities and took the ratio of the signals from both NO_2 and NO_3 absorption obtained with and without mirror purge flow. Averaging the ratios across both analytes and three separate experiments result in effective cavity lengths ($\pm 2\sigma$) of (59.7 ± 1.1) cm and (60.3 ± 0.9) cm for the NO_3 and N_2O_5 channel, respectively. Note that both values are, within their associated uncertainties, consistent with the reduction of the geometric cavity length to 60.6 cm and 60.3 cm, respectively, predicted from the cavity-to-sample-flow ratio (i.e. the pure dilution effect).

3.2 The mirror reflectivity

Equation (1) emphasizes the need of precise knowledge of the wavelength-dependent mirror reflectivity $R(\lambda)$. The two most common methods to determine $R(\lambda)$ include: (i) measuring a known concentration of a stable absorbing gas compound (Venables et al., 2006; Ventrillard-Courtillot et al., 2010), and (ii) measuring the ring-down time or the phase shift (Ball et al., 2004; Kennedy et al., 2011; Langridge et al., 2008). In this study we use the first method by purging the cavities with NO_2 taking advantage of its absorption across the entire spectral region of the LED emission, its well-known absorption cross sections σ_{NO_2} (in cm^2 $molecule^{-1}$) as well as its precisely known concentrations injected from the gas cylinder (N_{NO_2} in molecule cm^{-3}) thanks to the coupled NO_2 analyzer directly measuring each cell outflow during the calibration process (Fig.1

dashed black lines). Together with d_{eff} (section 3.1) and the directly measured transmission $T(\lambda)$, the reflectivity $R(\lambda)$ is deduced using Eq. (5):

$$R(\lambda) = 1 - \left(d_{eff}\sigma_{NO_2}N_{NO_2}\frac{T(\lambda)}{1-T(\lambda)}\right) \quad (5)$$

To compensate for the weak absorption cross-section of NO_2 in the 660–670 nm spectral range (Fig. 2b, orange), high NO_2 mixing ratios (400–800 ppbv) were used to reduce the uncertainty in the mirror reflectivity determination. Figure 3 shows representative wavelength-dependent reflectivity measurements for both cavities. Between 640 nm and 670 nm, $R(\lambda)$ ranged from 99.9866 % to 99.9886 % in the NO_3 cavity (blue points) and from 99.9768 % to 99.9837 % in the N_2O_5 cavity (orange points). Linear regression (solid lines) of the reflectivity yielded (1.18 ± 1.58) x 10^{-8} nm^{-1} x λ + 99.987% and (4.81 ± 0.75) x 10^{-8} nm^{-1} x λ + 99.949%. The slope for the NO_3 cavity is not significantly different from zero, indicating no evidence for a systematic wavelength dependence of R over the investigated spectral range. In contrast, the N_2O_5 cavity exhibits a statistically significant positive slope. Given the relatively small magnitude, the scatter of this variation and the greater uncertainty in the NO_2 absorption cross sections at 353 K compared with 298 K, the observed wavelength dependence may partly reflect systematic uncertainties in the reflectivity determination rather than an intrinsic wavelength dependence of R.

At 662 nm, corresponding to the NO_3 maximum absorption, the reflectivity was found to be 99.988 % for the NO_3 channel and 99.984 % for the N_2O_5 channel, in good agreement with the manufacturer's specifications ((99.98 ± 0.01) % at 630–690 nm). The corresponding overall optical path lengths $L(\lambda)$ were calculated with d/(1–$R(\lambda)$) as 5.1 km and 3.8 km, for the NO_3 and N_2O_5 channel, respectively.

Mirror reflectivity was also found to depend strongly on mirror cleanliness. During the ACROSS campaign (the instrument's first field deployment), the reflectivity at 662 nm varied between 99.983 % and 99.988 % for the NO_3 channel, corresponding to changes in L by a factor of 0.7, underlining the necessity of daily (or even more frequent) mirror reflectivity measurements.

3.3 The thermal dissociation of N_2O_5

Detection of ambient N_2O_5 requires its thermal dissociation to NO_3 via the TDI mentioned in Section 2.2. To determine the TDI heater temperature needed for quantitative N_2O_5 conversion, we coupled our NO_3 source upstream of the TDI and the N_2O_5 cavity, varying the TDI setpoint temperature between 300 and 473 K while recording the signal in the unheated N_2O_5 cavity, which thus served solely to characterize TDI conversion efficiency. The resulting NO_3 signal as a function of TDI temperature (the "thermogram") is shown in Fig. 4 (black points). N_2O_5 dissociation increases continuously above 300 K, reaching a maximum at 373 K; above this temperature, the signal decreases following a sigmoidal shape before levelling off between 450 and 475 K.

This behaviour prompted us trying to reproduce the observation and to run numerical simulation using FACSIMILE (Curtis and Sweetenham, 1987) based on the residence time in the TDI and cavity (derived from their volumes and the flow rate) together with the relevant reaction rate coefficients, including the NO_3–N_2O_5–NO_2 thermal equilibrium (k_2 and k_3, IUPAC (2026)), NO_3 thermolysis (k_8, Womack et al., 2017) and an NO_3 wall loss reaction (R9):

$$NO_3 + M \xrightarrow{\Delta} NO_2 + O + M \quad \text{(R8)}$$

$$NO_3 + surface \rightarrow products \quad \text{(R9)}$$

In order to verify if our observations are consistent with known gas-phase chemistry, we set k_9 to 0 s^{-1} in Model 1 (Fig. 4, orange). This model reproduces the N_2O_5 dissociation up to 373 K very well, but predicts a plateau beyond the maximum, since NO_3 thermolysis only becomes significant above 600 K – implying that a heterogeneous process, active only above 373 K, must be responsible for the observed decline. We reproduced the observations empirically with Model 2 by adding a Hill-type, temperature-dependent wall-loss term $k_9 = k_{Hill}(T) = 0.1\ s^{-1} + (0.3 \times T^{25} / (410^{25} + T^{25}))$: an arbitrarily chosen constant background loss (0.1 s^{-1}) between 300 and 373 K, followed by a sigmoidal increase in k_9 to 0.4 s^{-1} between 373 and 473 K. Such behaviour is consistent with a surface process governed by an activation barrier – for instance, the desorption of a passivating layer once a threshold temperature is exceeded. The background loss of 0.1 s^{-1} is consistent with the wall loss we estimated for our unheated NO_3 cavity (see below) while the high temperature wall loss of 0.4 s^{-1} appears plausible considering that previous studies report NO_3 wall loss rates that are 3–4 times higher in heated Teflon (or Teflon-coated) tubes than in their unheated equivalents (Sobanski et al., 2016; Türk et al., 2026). We find that 95 °C (grey dashed line) is the optimal TDI temperature, as it guarantees quantitative N_2O_5 conversion and lower NO_3 wall losses.

N_2O_5 detection typically relies on quantitative thermal conversion to NO_3 at a fixed, elevated temperature, with TDI temperature commonly verified by calculating the thermal N_2O_5 lifetime or via thermograms based on NO_2 (Friedrich et al., 2020; Womack et al., 2017), but rarely on NO_3 detection (Dubé et al., 2006; Fuchs et al., 2008). Dubé et al. (2006) determined the conversion efficiency at temperatures up to only 150°C and saw a marginal decrease above 130 °C. Fuchs et al. (2008) focused on the interplay of sampling flow, TDI temperature and conversion efficiency rather than discussing thermograms at a fixed flowrate. The behaviour observed here underscores the importance of thoroughly verifying the optimal TDI temperature based on NO_3 detection, as done in this study.

3.4 Losses of NO_3 during sampling

NO_3 is a highly reactive radical prone to surface losses during sampling. While inert materials (PFA, FEP, halocarbon wax) and short residence times minimize these losses, they remain a significant artefact in cavity systems (Fuchs et al., 2008). NO_3 (and N_2O_5) can be lost on: (1) PFA inlet tubing, (2) the filter holder, (3) the membrane inlet filter, and (4) the cavity (and TDI, for the N_2O_5 channel). Losses on PFA sampling lines are reported to be negligible and are typically disregarded by keeping residence times short relative to the cavity via minimal tubing length or high bypass flow (Crowley et al., 2011; Kennedy et al., 2011; Türk et al., 2026). The same applies to our filter holder: We observed no alteration in the NO_3 signal whether sampling was performed through it or through a 15 cm ¼ in. PFA tubing. Losses on the PTFE inlet filter type we deploy (Pall Corporation, R2PJ047) are very common and have been characterized repeatedly during the past 25 years, with reported transmission values reproducibly ranging between 86 % and 98% (Brown et al., 2002; Crowley et al., 2010; Dubé et al., 2006; Nam et al., 2022; Türk et al., 2026). The most recent estimate from Türk et al. (2026) reports a transmission efficiency of (90

± 5) % during field operation. By repeatedly switching between sampling NO_3 from CESAM through PFA tubing and through a clean filter, we found a transmission efficiency (± 2σ) of (90 ± 1) %, thereby confirming previous estimates (Fig. S3). We therefore selected this value for our correction factor calculation, i.e. T_{Filter} is 0.9 in both channels. Direct heterogeneous N_2O_5 losses on Teflon-coated surfaces are negligible relative to NO_3 losses and are therefore commonly excluded from the correction procedure (Fuchs et al., 2008; Kennedy et al., 2011; Türk et al., 2026).

To complete the correction scheme, we estimated the wall loss rate in the NO_3 cavity and the combined wall loss rate of TDI + N_2O_5 cavity. The NO_3 source was coupled to each cavity in turn, and residence time was varied via the cavity flow rate as previously demonstrated (Fuchs et al., 2008; Sobanski et al., 2016; Türk et al., 2026); for the NO_3 cavity, the TDI was positioned between source and cavity to boost NO_3 concentrations. Figure 5a shows the resulting exponential decay in NO_3 with increasing residence time in the NO_3 cavity. Since the NO_3/NO_2 mixture is not in thermal equilibrium upon entering the cavity, the decay was simulated with our box model from above (including k_2 and k_3 only), adjusting the initial NO_3 value to match the first data point. The dashed blue curve shows the signal decrease expected from equilibration alone, which fails to reproduce the data; varying the NO_3 wall loss rate to best-fit the observations (orange line) yields (0.10 ± 0.02) s^{-1}. With our residence time in the NO_3 cavity of 1.53 s, this results in a transmission efficiency $T_{\mathrm{NO_3\ channel}}$ of (88 ± 2) %.

The same approach was applied to the TDI + N_2O_5 cavity ensemble (latter thermostated at 80 °C), and repeated at three TDI temperatures (Fig. 5b) to qualitatively validate the wall-loss hypothesis underlying the N_2O_5 thermogram (Fig. 4, blue curve). Here, no equilibrium correction is needed, so effective wall loss rates were derived directly from the slopes (±2σ) of linear regressions: (0.26 ± 0.02), (0.27 ± 0.03), and (0.65 ± 0.11) s^{-1} at TDI temperatures of 80, 95, and 200 °C, respectively – corresponding to transmission efficiencies $T_{\mathrm{N_2O_5\ channel}}$ of (64 ± 2), (63 ± 3), and (34 ± 6) %. Note that even though the thermogram (Fig. 4) implies incomplete N_2O_5 conversion at 80°C, numerical simulations suggest quantitative dissociation within the first 0.2 s (from overall residence time 1.31 s) inside the heated cavity, suggesting that the linear regression approach is appropriate even at that temperature. The results in Fig. 5b are consistent with the thermogram: wall loss rates show no significant increase between 353 and 368 K, but increase 2.5-fold at 473 K. Note that we cannot directly implement the measured wall loss rates from Fig. 5b in the box model since the N_2O_5 cavity was unheated when measuring the thermogram. This reinforces the need to carefully select the TDI temperature to avoid unnecessarily large correction factors and the associated increase in measurement uncertainty. Recall that for freshly formed NO_3 in the TDI, k_{Wall} only applies to the residence time in the cavity leading to slightly higher transmissions $T^*_{\mathrm{N_2O_5\ channel}}$ of (67 ± 2), (66 ± 3) and (37 ± 6) %, at temperatures of 80, 95, and 200 °C, respectively.

3.5 Performance

The experiments presented above establishes the instrument response and the correction procedures required to account for sampling artifacts, including wall losses. With these effects quantified, the analytical performance of the instrument can now be assessed in terms of detection limits and overall measurement uncertainty.

3.5.1 Allan deviation and detection limits

The intrinsic detection capability of the instrument was estimated using overlapping Allan deviation analysis, which characterizes signal stability as a function of integration (averaging) time τ. For this purpose, both cavities were continuously flushed with dry zero air, and 1778 consecutive spectra with a sampling rate of 1 s were recorded under stable laboratory conditions. After converting the measured transmissions to NO_3 equivalents applying Eq. (1) and fitting with σ_{NO_3}, the overlapping Allan deviation was calculated using *AllanTools.py* (version 2024.4).

The resulting Allan deviation curves for the NO_3 and N_2O_5 channel under typical measurement conditions are shown in Fig. 6. Increasing the integration time initially decreases the Allan deviation in both channels, as expected, with a slope of ca. $1/\sqrt{\tau}$ because uncorrelated fluctuations in transmission (white noise) are progressively reduced through averaging. At longer integration times, however, slow instrumental drifts – arising from factors such as LED intensity fluctuations, cavity alignment and variations in pressure and temperature – become increasingly important, causing the Allan deviation to rise. The minimum of the Allan deviation therefore defines the optimum integration time reconciling averaging and drift effect and the corresponding noise-limited limit of detection achievable under these controlled conditions. Above 10 s, the two channels diverge: the N_2O_5 channel remains stable up to 100 s, whereas drift degrades the NO_3 channel LOD beyond 30 s. During the data acquisition period, the internal NO_3 cavity temperature increased by 0.6 °C. While the absence of temperature regulation in the NO_3 cavity may lead to temperature-induced misalignment, potentially explaining its lower long-term stability compared to the N_2O_5 cavity, other sources of slow instrumental drift may also contribute to this observation. The long-term oscillations in the N_2O_5 Allan plot likely reflect heating cycles from the temperature controller. Overall, Fig. 6 indicates an optimal compromise integration time of 15 s, yielding noise-limited LODs (LOD_{noise}) of 1.5 pptv (NO_3) and 2.2 pptv (N_2O_5). This analysis assumes that the mirror reflectivity remains constant. Drift effects, contamination and cleaning can additionally lead to a variability in R, thereby additionally affecting the LOD. For instance, over the entire ACROSS campaign, the standard deviation (1σ) of (1–R) from consecutive reflectivity estimations serving as measure for its variability was 21 % for the NO_3 channel and 27 % for the N_2O_5 channel. Propagating these 1σ variabilities into the Allan deviation analysis gives upper limits for LOD_{noise} of 1.8 pptv (NO_3) and 2.8 pptv (N_2O_5). The effect of the (1–R) variability on LOD_{noise} is represented by the shaded areas in Fig. 6.

As described in section 2.2, NO_3 (and N_2O_5) concentrations are estimated by spectral fitting. Due to the spectral interference with NO_2 and H_2O, both of which are usually present alongside NO_3 and N_2O_5 in ambient air, the LOD is likely to be worse under field conditions. Even though it is well known that both NO_2 and water vapour can influence the NO_3 retrieval performance of the fitting routine (Nam et al., 2022; Wang and Lu, 2019), to the best of our knowledge, their combined impact has not yet been systematically assessed. To investigate this effect, we were inspired by a synthetic-spectrum approach used to characterize fitting bias in other spectroscopic retrievals (e.g. Adkins and Hodges, 2022), here applied to IBBCEAS. Synthetic CEAS transmission spectra were generated using a rearranged form of Eq. (1), $T = [1 + \alpha(\lambda) \cdot d_{\mathrm{eff}} / (1 - R(\lambda))]^{-1}$, where α is directly computed from the laboratory reference cross-sections of NO_3 and NO_2 and the measured H_2O reference

spectrum via Eq. (2). Gaussian white noise, scaled from the Allan-deviation noise floor (LOD_{noise}) via the NO_3 reference spectrum, was added to $\alpha(\lambda)$ to yield an equivalent spectral noise level. Concentration combinations of NO_3 (0–10 pptv), NO_2 (0–50 ppbv), and H_2O (RH = 0.3–100% at 23°C) were drawn using a Latin Hypercube design (600 unique points, each with 10 independent noise realisations, giving 6000 spectra in total) (McKay et al., 1979) embedded in SciPy, and each synthetic spectrum was subsequently analysed with the same operational retrieval routine used for the ambient measurements.

Retrieved (averaged over the 10 noise realisations) vs. true NO_3 mixing ratios are shown in Fig. 7a and 7b, coloured by NO_2 and RH, respectively. As expected, the routine underperforms below LOD_{noise} (red dashed line), tending to overestimate NO_3, with scatter narrowing toward the 1:1 line (black dashed) at higher mixing ratios. This scatter shows no dependence on NO_2 (Fig. 7a) but correlates with RH (Fig. 7b). Plotting retrieval bias against NO_2 and RH (Fig. 7c and 7d) confirms this pattern: linear regression reveals no significant NO_2 dependence, but a modest negative trend with RH, corresponding to biases of + 0.49 to –0.71 pptv, comparable to the retrieval's inherent scatter (±0.64 pptv, 1σ). This suggests that the presence of H_2O and NO_2 biases the spectral fitting as soon as both are included as fitting parameters, with the bias showing only a marginal dependence on H_2O concentration and no apparent dependence on NO_2 concentration. Hence, instead of indicating an LOD depending on H_2O and NO_2, we prefer adding twice this inherent bias (2σ) across all 600 samples to LOD_{noise} resulting in an effective LOD of 3.2 pptv (solid black line, Fig. 7a and 7b), above which the data scatter symmetrically around the 1:1 line – consistent with this threshold representing a meaningful detection limit. The same analysis was carried out for the N_2O_5 channel, using the corresponding reference spectra and LOD_{noise} to generate a separate set of 6000 spectra; results are shown in the Supplement (Fig. S4). In this case, the bias decreases slightly with NO_2 and increases with RH, though again by a magnitude negligible compared to the fit-induced scatter. Using the standard deviation (2σ) of the mean bias yields an effective LOD of 4.4 pptv for the N_2O_5 channel. Note that this simulation approach only allows deduction of ballpark values as it neglects variability in both R and $\alpha_{H_2O}(T)$. For example, using the upper-limit values of LOD_{noise}, which account for variability in R results in worst-case (recall that R may fluctuate in both senses) effective LODs of 4.0 pptv (NO_3) and 5.8 pptv (N_2O_5). The synthetic spectra also show an RH-dependent NO_2 bias (Fig. S5, Supplement), which increases approximately linearly with RH by 0.20 (NO_3 channel) and 0.33 ppbv per % RH (N_2O_5 channel). For NO_3 above the LOD, this NO_2 bias is only weakly correlated with our above-mentioned NO_3 biases (r = –0.36 and +0.32 for the N_2O_5 and NO_3 channel, respectively), thereby confirming the low sensitivity of the NO_3 retrieval accuracy to NO_2 quantification. Nevertheless, taking advantage of the instrument's integrated CAPS analyzer, constraining NO_2 in the fit to measured values may allow reduction of the retrieval bias in both channels – especially under very humid conditions.

3.5.2 Total measurement uncertainty

Alongside the LOD, the total measurement uncertainty (TMU) is another important indicator of instrument performance. As is evident from Eqs. (1)–(3), the TMU of the NO_3 measurement is obtained by propagating, in quadrature (root-sum-square method), the relative uncertainties in: the retrieved N_{NO_3} from the spectral fitting procedure, the mirror reflectivity R, the

effective path length d_{eff}, the NO_3 absorption cross-section σ_{NO_3}, and the NO_3 transmission through the filter (T_{Filter}) and cavity ($T_{NO_3\ \mathrm{channel}}$). This assumes the individual error sources are independent and uncorrelated.

The uncertainty in N_{NO_3} from the spectral fitting procedure is accessible via the relative bias, the ratio of absolute bias to true NO_3 mixing ratio, derived from the simulated spectra in the previous section. This relative bias for the NO_3 channel is plotted against the true NO_3 mixing ratio in Fig. 8. It decreases exponentially with increasing NO_3 mixing ratio and approaches a constant systematic bias above the effective LOD. We captured this trend by binning the data and fitting a biexponential decay; the y-offset of the fit gives the relative fitting uncertainty, found to be 6.7%.

The relative uncertainty in the mirror reflectivity R is derived from Eq. (5) by propagating the relative uncertainties in d_{eff} (1.8 %), σ_{NO_2} at 298 K (3 %), N_{NO_2} concentration (0.5 %), and the spectral transmission (6 %, from the Allan deviation analysis), giving 7 %. Propagating this together with the uncertainties in d_{eff}, σ_{NO_3} (5 % at 298 K), T_{Filter} (5 %, Türk et al. (2026)), and $T_{NO_3\ \mathrm{channel}}$ (2 %) yields an overall TMU of 12% for [NO_3].

The same approach applies to the combined NO_3 + N_2O_5 signal $N_{NO_3+N_2O_5}$ measured in the N_2O_5 channel. Repeating the Fig. 8 analysis for this channel (Fig. S6, Supplement) gives a relative fitting uncertainty of 9.9%.

Propagating this with the uncertainty in R (10 %, itself from 5 % in σ_{NO_2} at 353 K, 1.5 % in d_{eff}, and 9 % in the spectral transmission) and in σ_{NO_3} at 353 K (8%) yields a relative uncertainty of 17 % in the summed signal.

Because N_2O_5 is obtained by channel differencing (Eq. 4), its total uncertainty requires propagating absolute errors (indicated with Δ) and directly measured values, and is given by:

$$\Delta_{N_2O_5} = \sqrt{\left(\frac{\Delta_{N_{NO_3}+N_2O_5}}{T^*_{N_2O_5\ \mathrm{channel}}}\right)^2 + \left(\frac{T_{N_2O_5\ \mathrm{channel}}\,[NO_3]\Delta_{T_{\mathrm{Filter}}}}{T^*_{N_2O_5\ \mathrm{channel}}}\right)^2 + \left(\frac{T_{\mathrm{Filter}}T_{N_2O_5\ \mathrm{channel}}\Delta[NO_3]}{T^*_{N_2O_5\ \mathrm{channel}}}\right)^2 + \left([N_2O_5]\frac{\Delta T^*_{N_2O_5\ \mathrm{channel}}}{T^*_{N_2O_5\ \mathrm{channel}}}\right)^2 + \left(\frac{T_{Filter}[NO_3]\Delta T_{N_2O_5}}{T^*_{N_2O_5\ \mathrm{channel}}}\right)^2} \quad (6)$$

The uncertainty related to [N_2O_5] depends on the NO_3-N_2O_5 ratio. During the ACROSS campaign (see below), an average relative TMU of 21 % for N_2O_5 was found.

3.5.3 Comparison to other instruments

Table 1 compares the LOD and TMU of this instrument with previous closed-path, field-deployable IBBCEAS setups for NO_3 and N_2O_5.

Table 1. Comparison of our instrument's performance with those of selected other IBBCEAS setups.

Reference	NO_3 LOD, TMU	N_2O_5 LOD, TMU
Ball et al. (2004)	2.5 pptv (1σ, 516s), NA	-
Langridge et al. (2008)	1 pptv (1σ, 2s), NA	-
Ventrillard-Courtillot et al. (2010)	2 pptv (1σ, 400 s), NA	-
Kennedy et al. (2011)	0.17 pptv (1σ, 830 s), 11 % Field: 1.0 pptv (1σ, 1s)	0.2 pptv (1σ, 850 s), > 14% Field: 2.4 pptv (1σ, 1s)

Wang et al. (2017)	2.4 pptv (1σ, 1s), 19 %	2.7 pptv (1σ, 1s), 22-36 %
Nam et al. (2022)	1.4 pptv (1σ, 1s), 11 %	-
Ling et al. (2023)	1.99 pptv (1σ, 1s), 15 %	-
This work	**1.5 pptv, (1σ, 15s), 12 %** ***LOD*$_{eff}$: 3.2 pptv (1σ, 15s)**	**2.2 pptv (1σ, 15s), 21 %** ***LOD*$_{eff}$: 4.4 pptv (1σ, 15s)**

Direct comparison is complicated by differing averaging times: several instruments report LODs at 1 s (Ling et al., 2023; Nam et al., 2022; Wang et al., 2017) or second-to-few-second integration (Ball et al., 2004; Kennedy et al., 2011; Langridge et al., 2008; Ventrillard-Courtillot et al., 2010), whereas our LOD is reported at 15 s. Since LOD scales approximately with the inverse square root of averaging time, our 1.5 pptv at 15 s corresponds to a higher 1 s-equivalent LOD, indicating that, while not the most sensitive system in this comparison, this instrument's noise-limited performance remains within the established range for closed-path IBB-CEAS instruments. Comparable or lower LODs at shorter integration times, as for example reported by Kennedy et al. (2011) and Nam et al. (2022), often go hand in hand with longer effective path lengths achieved through mirrors with higher reflectivity. However, higher mirror reflectivity reduces the intensity reaching the detector, so that increasing R does not necessarily improve the LOD (Vaughan et al., 2008). Our choice of mirror reflectivity and cavity length represents a compromise between sensitivity, transmitted intensity, mechanical stability and cost.

More directly comparable is the TMU, which varies less sensitively with averaging time. Here, our value of 12 % for NO_3 is in good agreement with Kennedy et al. (2011, 11 %) and Nam et al. (2022, 11 %), and notably lower than Wang et al. (2017, 19 %). For N_2O_5, our mean TMU of 21 % is comparable to the lower end of the range reported by Kennedy et al. (2011, >14%) and Wang et al. (2017, 22–36%). This indicates that our systematic uncertainty of our retrieval is competitive with previously reported closed-path IBB-CEAS instruments.

Importantly, the effective (field-relevant) LODs reported here, 3.2 pptv for NO_3 and 4.4 pptv for N_2O_5, already account for the fitting-induced bias identified in section 3.5.1, which to our knowledge has not been systematically quantified in prior studies. Kennedy et al. (2011) reported effective LODs deduced from daytime ambient measurements. Other works report only a noise-limited LOD, however the true field detection limit may in practice be similarly elevated. The analysis presented here suggests that noise-limited LODs alone may understate the effective detection threshold achievable under realistic ambient conditions.

4 Field deployment

The NOyBOx instrument was deployed for the first time during the ACROSS campaign (Cantrell and Michoud, 2022), which took place over one month in summer 2022. The instrument was set up atop a 40 m tower amid and above the canopy (16–20 m) of the Rambouillet forest, ca. 50 km from Paris – a site dominated by biogenic emissions but occasionally impacted by urban plumes emanating from Paris. The IBBCEAS subsystem was operated as detailed in Section 2.2, but with a 120 s integration time and a TDI temperature of 473 K; R and I_0 were determined every 24 h and 1–1.5 h, respectively, and inlet

filters were changed manually every 4–6 h. The N_2O_5 inlet filter was positioned between the TDI and the cavity during that period, which is why Eq. (4) was modified accordingly to retrieve N_2O_5 mixing ratios. A power outage disabled our NO analyzer, so NO was instead measured with another chemiluminescence instrument (T200U, Aerodyne; LOD = 30 pptv) operated by IMT Nord Europe. The NO_y and NO_2 analyzers were operated as described in Section 2.1, allowing NO_y to be derived as well. O_3 was monitored by a UV absorption instrument (HORIBA APOA-370, LOD = 2.5 ppbv), and temperature was measured at 5 m and 41 m along the tower (Atexis PT1000 and Thermoset PT100) by CNRM (Météo-France).

Figure 9 shows the time series of a representative night (16 – 17 July 2022) from this campaign. Note that NO_3 levels were additionally corrected by a factor of 0.94 on average using our box model introduced in Sect. 3.3. This accounts for further NO_3 formed by N_2O_5 dissociation (R3) during the residence time in the cavity, which was ca. 5 K warmer than ambient air (see Fig. S7, Supplement). O_3 decreased from 50 to 44 ppbv and NO_2 from 4.7 to 2.6 ppbv over the course of the night (panel a, right axis, blue); NO (panel c, right axis, grey) remained below the LOD until sunrise at ca. 05:30 LT. It was a mild summer night, with temperature (panel e, blue) decreasing from 292 to 289 K. NO_2 peaked at 4.7 ppbv at 00:30 LT, increasing the NO_3 production rate; by 01:00 LT, NO_3 and N_2O_5 reached 6 and 30 pptv, respectively (panel c). Despite the continued gradual decline in NO_2 and O_3 thereafter, NO_3 and N_2O_5 continued to increase through the night, coinciding with the onset of a temperature inversion ($\Delta T = T_{41\,m} - T_{5\,m}$, panel e, orange) reaching ca. 3 K, in which air atop the tower was warmer than at ground level. As discussed in detail for this campaign by Dewald et al. (2024) and Andersen et al. (2024), such inversions decouple the tower from below-canopy reactive trace-gas emissions, reducing NO_3 reactivity – consistent with the observed rise in NO_3/N_2O_5. Peak mixing ratios of 12 pptv NO_3 and 182 pptv N_2O_5 were reached at 05:15 LT, shortly before both fell below the LOD around sunrise (05:30 LT).

Using our simultaneous NO_3, N_2O_5, and NO_2 measurements, we calculated $[N_2O_5]/([NO_3][NO_2])$ (panel b, orange) and compared it to the purely temperature-dependent value recommended equilibrium constant K_{eq} by JPL (Burkholder et al. (2025); blue line). The two agree fairly within uncertainties for most of the night, with only occasional deviations. Following Crowley et al. (2010), the time needed to reach equilibrium, $(k_2/k_3 \times [NO_2])^{-1}$, was 6–10 s on this night using IUPAC-recommended rate coefficients, so thermal equilibrium should be established essentially throughout. We attribute the initial disagreement to instrument line and filter passivation from priorly sampled highly reactive air, an effect also reported for other cavity-based setups (Crowley et al., 2011; Türk et al., 2026). The deviations at 04:30 LT can be reconciled with local disturbances of the NO_3–N_2O_5 equilibrium, for instance due to boundary-layer instabilities as reflected in the continuous breakdown of the temperature inversion (panel e), leading to sudden BVOC entrainment and very local NO_3/N_2O_5 sinks (Brown et al., 2003; Dewald et al., 2020). Indeed, Chen et al. (2022) confirmed systematically with simulations that a purely temperature-derived K_{eq} is expected to deviate substantially from the ambient $[N_2O_5]/([NO_3][NO_2])$ ratio when competing NO_3 and N_2O_5 sinks prevent the system from reaching true equilibrium.

NO_y remained stable at ca. 5 ppbv throughout the night (panel d, blue), indicating that deposition of newly formed NO_y species is negligible. NO_z (= $NO_y - NO_x$; panel d, orange) fell to zero between 00:00 and 01:00 LT, indicating that NO_x was the only reactive nitrogen species present at that time and pointing to a certain degree of decoupling from below-canopy emissions.

With the onset of NO_3 and N_2O_5 formation, 0.5–1 ppbv of NO_z was produced showing that NO_3 and N_2O_5 alone cannot close the NO_y budget. Indeed, these elevated NO_3, N_2O_5, and NO_y mixing ratios coincided with the detection of NO_3 + BVOC oxidation products by CIMS; this will be explored in a forthcoming publication.

This case study illustrates the broader value of combining NO_x, NO_y, and NO_3/N_2O_5 measurements within a single instrument. By simultaneously constraining NO_z production, we can directly assess how efficiently NO_3 and N_2O_5 are being converted into higher-generation products – as demonstrated here, where the observed NO_z increase accounted for only a fraction of the concurrent NO_3/N_2O_5 signal, pointing to additional, yet-unquantified oxidation pathways. For example, the NO_3-initiated oxidation of BVOCs can lead to the formation of organic nitrates, which themselves may be hydrolysed to contribute to HNO_3 production.

5 Summary and conclusions

We presented the design and characterization of the NOyBOx instrument, combining NO_x, NO_y, and IBBCEAS-based NO_3/N_2O_5 measurements within a single framework. The noise-limited and effective detection limits of the NO_3 and N_2O_5 channels were determined via Allan deviation analysis and a synthetic-spectra approach, yielding effective LODs in ambient air conditions of 3.2 pptv and 4.4 pptv, and total measurement uncertainties of 12 % and 21 %, respectively – performance competitive with previously reported closed-path IBBCEAS instruments. Moreover, using synthetic spectra spanning realistic ambient NO_2 and H_2O concentrations, we showed that spectral interference from these species can bias the NO_3/N_2O_5 retrieval beyond what is predicted by the noise-limited LOD alone. Accounting for this bias is essential to avoid underestimating the true detection threshold under field conditions, and we recommend that future IBBCEAS studies evaluate this effect explicitly rather than relying on noise-limited LODs alone.

A thermogram of N_2O_5 based on NO_3 detection was performed. With the exception of Dubé et al. (2006), which covers only the range between 70 and 150°C, no NO_3-based thermogram is available in the literature. Our study therefore provides the first complete NO_3-based thermogram of N_2O_5 over the temperature range of 30 to 200 °C, revealing substantially high wall losses at elevated temperatures. This finding underscores the necessity of characterizing the TDI for N_2O_5 dissociation based on NO_3 detection in order to prevent the application of unnecessarily high correction factors.

Finally, the instrument was successfully deployed for the first time during the ACROSS field campaign, thereby demonstrating the value of combining NO_x, NO_y, and NO_3/N_2O_5 within a single internally consistent framework. As inferred from our case study, NO_3-initiated chemistry formed a significant source of other NO_z species. Such observations, achievable only through co-located NO_x, NO_y, and NO_3/N_2O_5 measurements, is essential for constraining the fate of reactive nitrogen at night and represents a key advantage of the NOyBOx over instruments measuring these species in isolation.

Code and data availability

Data underlying the figures in this publication are available at Zenodo: https://doi.org/10.5281/zenodo.23922481 (Dewald et al., 2026b). Data from the ACROSS campaign is available at ACTRIS-AERIS (https://across.aeris-data.fr/, last access: 14 July 2026).

Author contributions

Conceptualization: SH, PD, MCi, BPV, MC, EP, MF, XL
Methodology: SH, PD, MCi, BPV
Formal analysis: SH, PD, MCi, BPV
Data curation/Investigation: SH, MCi, BPV, EP, MC, AB, VM, LB
Resources: CC, MC, EP, VM
Writing – Original Draft: SH, PD
Writing – Review and Editing: all authors
Visualization: PD
Project administration: MCi, CC, VM
Funding acquisition: MCi, BPV, CC

Competing interests

At least one of the (co-)authors serves as editor for the special issue to which this paper belongs.

Acknowledgements

The authors thank Olivier Garrouste and Cyrielle Denjean from CNRM (Météo-France) as well as Sébastien Dusanter and Marina Jamar from IMT Nord Europe for the provision of temperature and NO data, respectively. We further thank Pascal Zapf, Cécile Gaimoz and Franck Maisonneuve for assistance during the ACROSS campaign on the Rambouillet site. The ACROSS project has received funding from ANR under the investment program integrated into France 2030, with the reference ANR-17-MPGA-0002, and it has been supported by the French national program LEFE (Les Enveloppes Fluides et l'Environnement) of the CNRS INSU (Centre National de la Recherche Scientifique - Institut National des Sciences de l'Univers). This work has also been supported by the region "Ile de France" in the framework of a call for projects from DIM QI2 and by the Université Paris-Est Creteil investment founding. Data from the ACROSS campaign are hosted by the French national centre for atmospheric data and services, AERIS. The authors gratefully acknowledge CNRS-INSU, Université Paris-Est Créteil, Université Paris-Cité, and OSU-EFLUVE for supporting CESAM platform as a component of ACTRIS Research

Infrastructure. This platform also benefits from the support of ACTRIS-FR, registered on the Roadmap of the French Ministry of Research. The authors thank AERIS for curating and distributing the data produced by CESAM chamber through ACTRIS portal (https://dc.actris.nilu.no/) and ACTRIS DC ASC Unit (formerly known as EUROCHAMP DC, https://data.eurochamp.org). PD has received funding from the European Union's Horizon research and innovation programme under the Marie Skłodowska-Curie (Postdoctoral Fellowship) grant agreement No. 101206921 (NOCTEM project). This work was also supported by the French Environment and Energy Management Agency (ADEME).

References

Adkins, E. M. and Hodges, J. T.: Assessment of the precision, bias and numerical correlation of fitted parameters obtained by multi-spectrum fits of the Hartmann-Tran line profile to simulated absorption spectra, J. Quant. Spectrosc. Radiat. Transf., 280, 108100, https://doi.org/10.1016/j.jqsrt.2022.108100, 2022.

Aldener, M., Brown, S. S., Stark, H., Williams, E. J., Lerner, B. M., Kuster, W. C., Goldan, P. D., Quinn, P. K., Bates, T. S., Fehsenfeld, F. C., and Ravishankara, A. R.: Reactivity and loss mechanisms of NO_3 and N_2O_5 in a polluted marine environment: Results from in situ measurements during New England Air Quality Study 2002, J. Geophys. Res.-Atmos., 111, D23S73, https://doi.org/10.1029/2006JD007252, 2006.

Aliwell, S. R. and Jones, R. L.: Measurement of atmospheric NO_3 1. Improved removal of water vapour absorption features in the analysis for NO_3, Geophys. Res. Lett., 23, 2585–2588, https://doi.org/10.1029/96GL02472, 1996.

Andersen, S. T., McGillen, M. R., Xue, C., Seubert, T., Dewald, P., Türk, G. N. T. E., Schuladen, J., Denjean, C., Etienne, J. C., Garrouste, O., Jamar, M., Harb, S., Cirtog, M., Michoud, V., Cazaunau, M., Bergé, A., Cantrell, C., Dusanter, S., Picquet-Varrault, B., Kukui, A., Mellouki, A., Carpenter, L. J., Lelieveld, J., and Crowley, J. N.: Measurement report: Sources, sinks, and lifetime of NO_x in a suburban temperate forest at night, Atmos. Chem. Phys., 24, 11603–11618, https://doi.org/10.5194/acp-24-11603-2024, 2024.

Ball, S. M., Povey, I. M., Norton, E. G., and Jones, R. L.: Broadband cavity ringdown spectroscopy of the NO_3 radical, Chem. Phys. Lett., 342, 113–120, https://doi.org/10.1016/S0009-2614(01)00573-5, 2001.

Ball, S. M., Langridge, J. M., and Jones, R. L.: Broadband cavity enhanced absorption spectroscopy using light emitting diodes, Chem. Phys. Lett., 398, 68–74, https://doi.org/10.1016/j.cplett.2004.08.144, 2004.

Berden, G., Peeters, R., and Meijer, G.: Cavity ring-down spectroscopy: Experimental schemes and applications, Int. Rev. Phys. Chem., 19, 565–607, https://doi.org/10.1080/014423500750040627, 2000.

Bitter, M., Ball, S. M., Povey, I. M., and Jones, R. L.: A broadband cavity ringdown spectrometer for in-situ measurements of atmospheric trace gases, Atmos. Chem. Phys., 5, 2547–2560, https://doi.org/10.5194/acp-5-2547-2005, 2005.

Bolzacchini, E., Bruschi, M., Hjorth, J., Meinardi, S., Orlandi, M., Rindone, B., and Rosenbohm, E.: Gas-Phase Reaction of Phenol with NO_3, Environ. Sci. Technol., 35, 1791–1797, https://doi.org/10.1021/es001290m, 2001.

Brown, S. S.: Absorption spectroscopy in high-finesse cavities for atmospheric studies, Chem. Rev., 103, 5219–5238, https://doi.org/10.1021/cr020645c, 2003.

Brown, S. S. and Stutz, J.: Nighttime radical observations and chemistry, Chem. Soc. Rev., 41, 6405–6447, https://doi.org/10.1039/C2CS35181A, 2012.

Brown, S. S., Stark, H., and Ravishankara, A. R.: Cavity ring-down spectroscopy for atmospheric trace gas detection: application to the nitrate radical (NO_3), Appl. Phys. B, 75, 173–182, https://doi.org/10.1007/s00340-002-0980-y, 2002.

Brown, S. S., Stark, H., and Ravishankara, A. R.: Applicability of the steady state approximation to the interpretation of atmospheric observations of NO_3 and N_2O_5, J. Geophys. Res.-Atmos., 108, 4539, https://doi.org/10.1029/2003JD003407, 2003.

Brown, S. S., Dube, W. P., Osthoff, H. D., Wolfe, D. E., Angevine, W. M., and Ravishankara, A. R.: High resolution vertical distributions of NO_3 and N_2O_5 through the nocturnal boundary layer, Atmos. Chem. Phys., 7, 139–149, https://doi.org/10.5194/acp-7-139-2007, 2007.

Brown, S. S., Dube, W. P., Fuchs, H., Ryerson, T. B., Wollny, A. G., Brock, C. A., Bahreini, R., Middlebrook, A. M., Neuman, J. A., Atlas, E., Roberts, J. M., Osthoff, H. D., Trainer, M., Fehsenfeld, F. C., and Ravishankara, A. R.: Reactive uptake coefficients for N_2O_5 determined from aircraft measurements during the Second Texas Air Quality Study: Comparison to current model parameterizations, J. Geophys. Res.-Atmos., 114, D00F10, https://doi.org/10.1029/2008JD011679, 2009.

Brown, S. S., An, H., Lee, M., Park, J.-H., Lee, S.-D., Fibiger, D. L., McDuffie, E. E., Dubé, W. P., Wagner, N. L., and Min, K.-E.: Cavity enhanced spectroscopy for measurement of nitrogen oxides in the Anthropocene: results from the Seoul tower during MAPS 2015, Faraday Discuss., 200, 529–557, https://doi.org/10.1039/C7FD00001D, 2017.

Burkholder, J. B., Caravan, R. L., Huie, R. E., Orkin, V. L., Percival, C. J., Sander, R., Sander, S. P., and Wilmouth, D. M.: Chemical Kinetics and Photochemical Data for Use in Atmospheric Studies, Evaluation No. 20, JPL Publication 25-1, Jet Propulsion Laboratory, Pasadena, https://doi.org/10.48577/jpl.KFQ0TZ, 2025.

Cantrell, C. and Michoud, V.: An Experiment to Study Atmospheric Oxidation Chemistry and Physics of Mixed Anthropogenic–Biogenic Air Masses in the Greater Paris Area, Bull. Am. Meteorol. Soc., 103, 599–603, https://doi.org/10.1175/BAMS-D-21-0115.1, 2022.

Chen, X., Wang, H., and Lu, K.: Interpretation of NO_3–N_2O_5 observation via steady state in high-aerosol air mass: the impact of equilibrium coefficient in ambient conditions, Atmos. Chem. Phys., 22, 3525–3533, https://doi.org/10.5194/acp-22-3525-2022, 2022.

Clough, P. N. and Thrush, B. A.: Mechanism of chemiluminescent reaction between nitric oxide and ozone, Trans. Faraday Soc., 63, 915–925, https://doi.org/10.1039/TF9676300915, 1967.

Crowley, J. N., Schuster, G., Pouvesle, N., Parchatka, U., Fischer, H., Bonn, B., Bingemer, H., and Lelieveld, J.: Nocturnal nitrogen oxides at a rural mountain site in south-western Germany, Atmos. Chem. Phys., 10, 2795–2812, https://doi.org/10.5194/acp-10-2795-2010, 2010.

Crowley, J. N., Thieser, J., Tang, M. J., Schuster, G., Bozem, H., Hasaynali Beygi, Z., Fischer, H., Diesch, J.-M., Drewnick, F., Borrmann, S., Song, W., Yassaa, N., Williams, J., Pöhler, D., Platt, U., and Lelieveld, J.: Variable lifetimes and loss mechanisms for NO_3 and N_2O_5 during the DOMINO campaign: Contrast between marine, urban and continental air, Atmos. Chem. Phys., 11, 10863–10870, https://doi.org/10.5194/acp-11-10853-2011, 2011.

Crutzen, P. J. and Lelieveld, J.: Human impacts on atmospheric chemistry, Annu. Rev. Earth Planet. Sci., 29, 17–45, https://doi.org/10.1146/annurev.earth.29.1.17, 2001.

Curtis, A. R. and Sweetenham, W. P.: Facsimile, Atomic Energy Research Establishment, Report R-12805, Harwell Laboratory, Oxfordshire, UK, ISBN: 0705813177, 1987.

Davidson, J. A., Cantrell, C. A., McDaniel, A. H., Shetter, R. E., Madronich, S., and Calvert, J. G.: Visible-ultraviolet absorption cross sections for NO_2 as a function of temperature, J. Geophys. Res. Atmos., 93, 7105–7112, https://doi.org/10.1029/JD093iD06p07105, 1988.

Day, D. A., Wooldridge, P. J., Dillon, M. B., Thornton, J. A., and Cohen, R. C.: A thermal dissociation laser-induced fluorescence instrument for in situ detection of NO_2, peroxy nitrates, alkyl nitrates, and HNO_3, J. Geophys. Res.-Atmos., 107, https://doi.org/10.1029/2001jd000779, 2002.

Dewald, P., Liebmann, J. M., Friedrich, N., Shenolikar, J., Schuladen, J., Rohrer, F., Reimer, D., Tillmann, R., Novelli, A., Cho, C. M., Xu, K. M., Holzinger, R., Bernard, F., Zhou, L., Mellouki, W., Brown, S. S., Fuchs, H., Lelieveld, J., and Crowley, J. N.: Evolution of NO_3 reactivity during the oxidation of isoprene, Atmos. Chem. Phys., 20, 10459–10475, https://doi.org/10.5194/acp-20-10459-2020, 2020.

Dewald, P., Seubert, T., Andersen, S. T., Türk, G. N. T. E., Schuladen, J., McGillen, M. R., Denjean, C., Etienne, J. C., Garrouste, O., Jamar, M., Harb, S., Cirtog, M., Michoud, V., Cazaunau, M., Bergé, A., Cantrell, C., Dusanter, S., Picquet-Varrault, B., Kukui, A., Xue, C., Mellouki, A., Lelieveld, J., and Crowley, J. N.: NO_3 reactivity during a summer period in a temperate forest below and above the canopy, Atmos. Chem. Phys., 24, 8983–8997, https://doi.org/10.5194/acp-24-8983-2024, 2024.

Dewald, P., Seubert, T., Wüst, L., Schuladen, J., Drewnick, F., Fachinger, F., Hoffmann, T., and Crowley, J. N.: Particle nitrate measurement using a thermal-dissociation, cavity-ringdown-spectrometer with gas-phase denuder (D-TD-CRDS), Atmos. Meas. Tech., 19, 3445–3457, https://doi.org/10.5194/amt-19-3445-2026, 2026a.

Dewald, P., Harb, S., Picquet-Varrault, B., Cazaunau, M., Feingesicht, M., Beltran, L., Michoud, V., Landsheere, X., Pangui, E., Bergé, A., Cantrell, C., and Cirtog, M.: Data underlying the figures of "An incoherent broadband cavity-enhanced absorption spectrometer for simultaneous NO_3 and N_2O_5 measurements, integrated into a NO_y instrument suite: characterization and first field deployment", Zenodo [dataset], https://doi.org/10.5281/zenodo.23922482, 2026b.

Dorn, H. P., Apodaca, R. L., Ball, S. M., Brauers, T., Brown, S. S., Crowley, J. N., Dubé, W. P., Fuchs, H., Häseler, R., Heitmann, U., Jones, R. L., Kiendler-Scharr, A., Labazan, I., Langridge, J. M., Meinen, J., Mentel, T. F., Platt, U., Pöhler, D., Rohrer, F., Ruth, A. A., Schlosser, E., Schuster, G., Shillings, A. J. L., Simpson, W. R., Thieser, J., Tillmann, R., Varma, R., Venables, D. S., and Wahner, A.: Intercomparison of NO_3 radical detection instruments in the atmosphere simulation chamber SAPHIR, Atmos. Meas. Tech., 6, 1111–1140, https://doi.org/10.5194/amt-6-1111-2013, 2013.

Dubé, W. P., Brown, S. S., Osthoff, H. D., Nunley, M. R., Ciciora, S. J., Paris, M. W., McLaughlin, R. J., and Ravishankara, A. R.: Aircraft instrument for simultaneous, in situ measurement of NO_3 and N_2O_5 via pulsed cavity ring-down spectroscopy, Rev. Sci. Instrum., 77, https://doi.org/10.1063/1.2176058, 2006.

Dutta, I., Heald, C. L., Bourgeois, I., Crounse, J. D., Hintsa, E. J., Moore, F. L., and Peischl, J.: Characterizing the Global Tropospheric Budget of Oxidized Nitrogen (NO_y), EGUsphere, 2026, 1–28, https://doi.org/10.5194/egusphere-2026-875, 2026.

Engeln, R., Berden, G., Peeters, R., and Meijer, G.: Cavity enhanced absorption and cavity enhanced magnetic rotation spectroscopy, Rev. Sci. Instrum., 69, 3763–3769, https://doi.org/10.1063/1.1149176, 1998.

Fahey, D. W., Hübler, G., Parrish, D. D., Williams, E. J., Norton, R. B., Ridley, B. A., Singh, H. B., Liu, S. C., and Fehsenfeld, F. C.: Reactive Nitrogen Species in the Troposphere: Measurements of NO, NO_2, HNO_3, Particulate Nitrate, Peroxyacetyl

Nitrate (PAN), O_3, and Total Reactive Odd Nitrogen (NO_y) at Niwot Ridge, Colorado, J. Geophys. Res., 91, 9781–9793, https://doi.org/10.1029/JD091iD09p09781, 1986.

Fiedler, S. E., Hese, A., and Ruth, A. A.: Incoherent broad-band cavity-enhanced absorption spectroscopy, Chem. Phys. Lett., 371, 284–294, https://doi.org/10.1016/S0009-2614(03)00263-X, 2003.

Finlayson-Pitts, B. J. and Pitts, J. N.: CHAPTER 7 - Chemistry of Inorganic Nitrogen Compounds, in: Chemistry of the Upper and Lower Atmosphere, edited by: Finlayson-Pitts, B. J. and Pitts, J. N., Academic Press, San Diego, 264–293, https://doi.org/10.1016/B978-012257060-5/50009-5, 2000.

Fouqueau, A., Cirtog, M., Cazaunau, M., Pangui, E., Zapf, P., Siour, G., Landsheere, X., Méjean, G., Romanini, D., and Picquet-Varrault, B.: Implementation of an incoherent broadband cavity-enhanced absorption spectroscopy technique in an atmospheric simulation chamber for in situ NO_3 monitoring: characterization and validation for kinetic studies, Atmos. Meas. Tech., 13, 6311–6323, https://doi.org/10.5194/amt-13-6311-2020, 2020.

Friedrich, N., Tadic, I., Schuladen, J., Brooks, J., Darbyshire, E., Drewnick, F., Fischer, H., Lelieveld, J., and Crowley, J. N.: Measurement of NOx and NOy with a thermal dissociation cavity ring-down spectrometer (TD-CRDS): instrument characterisation and first deployment, Atmos. Meas. Tech., 13, 5739–5761, https://doi.org/10.5194/amt-13-5739-2020, 2020.

Fry, J. L., Draper, D. C., Barsanti, K. C., Smith, J. N., Ortega, J., Winkle, P. M., Lawler, M. J., Brown, S. S., Edwards, P. M., Cohen, R. C., and Lee, L.: Secondary Organic Aerosol Formation and Organic Nitrate Yield from NO_3 Oxidation of Biogenic Hydrocarbons, Environ. Sci. Technol., 48, 11944–11953, https://doi.org/10.1021/es502204x, 2014.

Fuchs, H., Dube, W. P., Cicioira, S. J., and Brown, S. S.: Determination of inlet transmission and conversion efficiencies for in situ measurements of the nocturnal nitrogen oxides, NO_3, N_2O_5 and NO_2, via pulsed cavity ring-down spectroscopy, Anal. Chem., 80, 6010–6017, https://doi.org/10.1021/ac8007253, 2008.

Fuchs, H., Ball, S. M., Bohn, B., Brauers, T., Cohen, R. C., Dorn, H. P., Dube, W. P., Fry, J. L., Haseler, R., Heitmann, U., Jones, R. L., Kleffmann, J., Mentel, T. F., Musgen, P., Rohrer, F., Rollins, A. W., Ruth, A. A., Kiendler-Scharr, A., Schlosser, E., Shillings, A. J. L., Tillmann, R., Varma, R. M., Venables, D. S., Tapia, G. V., Wahner, A., Wegener, R., Wooldridge, P. J., and Brown, S. S.: Intercomparison of measurements of NO_2 concentrations in the atmosphere simulation chamber SAPHIR during the NO_3-Comp campaign, Atmos. Meas. Tech., 3, 21–37, https://doi.org/10.5194/amt-3-21-2010, 2010.

Ge, B., Sun, Y., Liu, Y., Dong, H., Ji, D., Jiang, Q., Li, J., and Wang, Z.: Nitrogen dioxide measurement by cavity attenuated phase shift spectroscopy (CAPS) and implications in ozone production efficiency and nitrate formation in Beijing, China, J. Geophys. Res. Atmos., 118, 9499–9509, https://doi.org/10.1002/jgrd.50757, 2013.

Geyer, A., Alicke, B., Konrad, S., Schmitz, T., Stutz, J., and Platt, U.: Chemistry and oxidation capacity of the nitrate radical in the continental boundary layer near Berlin, J. Geophys. Res.-Atmos., 106, 8013–8025, https://doi.org/10.1029/2000jd900681, 2001a.

Geyer, A., Ackermann, R., Dubois, R., Lohrmann, B., Muller, T., and Platt, U.: Long-term observation of nitrate radicals in the continental boundary layer near Berlin, Atmos. Environ., 35, 3619–3631, https://doi.org/10.1016/S1352-2310(00)00549-5, 2001b.

Gherman, T., Venables, D. S., Vaughan, S., Orphal, J., and Ruth, A. A.: Incoherent broadband cavity-enhanced absorption spectroscopy in the near-ultraviolet: Application to HONO and NO_2, Environ. Sci. Technol., 42, 890–895, https://doi.org/10.1021/es0716913, 2008.

Hosaynali Beygi, Z., Fischer, H., Harder, H. D., Martinez, M., Sander, R., Williams, J., Brookes, D. M., Monks, P. S., and Lelieveld, J.: Oxidation photochemistry in the Southern Atlantic boundary layer: unexpected deviations of photochemical steady state, Atmos. Chem. Phys., 11, 8497–8513, https://doi.org/10.5194/acp-11-8497-2011, 2011.

Hu, H., Wang, H., Lu, K., Wang, J., Zheng, Z., Xu, X., Zhai, T., Chen, X., Lu, X., Fu, W., Li, X., Zeng, L., Hu, M., Zhang, Y., and Fan, S.: Variation and trend of nitrate radical reactivity towards volatile organic compounds in Beijing, China, Atmos. Chem. Phys., 23, 8211–8223, https://doi.org/10.5194/acp-23-8211-2023, 2023.

Ito, A., Sillman, S., and Penner, J. E.: Effects of additional nonmethane volatile organic compounds, organic nitrates, and direct emissions of oxygenated organic species on global tropospheric chemistry, J. Geophys. Res. Atmos., 112, https://doi.org/10.1029/2005JD006556, 2007.

IUPAC: Task Group on Atmospheric Chemical Kinetic Data Evaluation, edited by: Ammann, M., Cox, R.A., Crowley, J.N., Herrmann, H., Jenkin, M.E., McNeill, V.F., Mellouki, A., Rossi, M. J., Troe, J. and Wallington, T. J., https://iupac.aeris-data.fr/, last access: 13th July 2026.

Javed, U., Kubistin, D., Martinez, M., Pollmann, J., Rudolf, M., Parchatka, U., Reiffs, A., Thieser, J., Schuster, G., Horbanski, M., Pöhler, D., Crowley, J. N., Fischer, H., Lelieveld, J., and Harder, H.: Laser-induced fluorescence-based detection of atmospheric nitrogen dioxide and comparison of different techniques during the PARADE 2011 field campaign, Atmos. Meas. Tech., 12, 1461–1481, https://doi.org/10.5194/amt-12-1461-2019, 2019.

Kane, S. M., Caloz, F., and Leu, M.-T.: Heterogeneous Uptake of Gaseous N_2O_5 by $(NH_4)_2SO_4$, NH_4HSO_4, and H_2SO_4 Aerosols, J. Phys. Chem. A, 105, 6465–6470, https://doi.org/10.1021/jp010490x, 2001.

Kebabian, P. L., Herndon, S. C., and Freedman, A.: Detection of Nitrogen Dioxide by Cavity Attenuated Phase Shift Spectroscopy, Anal. Chem., 77, 724–728, https://doi.org/10.1021/ac048715y, 2005.

Keller-Rudek, H., Moortgat, G. K., Sander, R., and Sörensen, R.: The MPI-Mainz UV/VIS Spectral Atlas of Gaseous Molecules of Atmospheric Interest, Earth. Syst. Sci. Data, 5, 365–373, https://doi.org/10.5194/essd-5-365-2013, 2013.

Kennedy, O. J., Ouyang, B., Langridge, J. M., Daniels, M. J. S., Bauguitte, S., Freshwater, R., McLeod, M. W., Ironmonger, C., Sendall, J., Norris, O., Nightingale, R., Ball, S. M., and Jones, R. L.: An aircraft based three channel broadband cavity enhanced absorption spectrometer for simultaneous measurements of NO_3, N_2O_5 and NO_2, Atmos. Meas. Tech., 4, 1759–1776, https://doi.org/10.5194/amt-4-1759-2011, 2011.

Kercher, J. P., Riedel, T. P., and Thornton, J. A.: Chlorine activation by N_2O_5: simultaneous, in situ detection of $ClNO_2$ and N_2O_5 by chemical ionization mass spectrometry, Atmos. Meas. Tech., 2, 193–204, https://doi.org/10.5194/amt-2-193-2009, 2009.

Kiendler-Scharr, A., Mensah, A. A., Friese, E., Topping, D., Nemitz, E., Prevot, A. S. H., Äijälä, M., Allan, J., Canonaco, F., Canagaratna, M., Carbone, S., Crippa, M., Dall Osto, M., Day, D. A., De Carlo, P., Di Marco, C. F., Elbern, H., Eriksson, A., Freney, E., Hao, L., Herrmann, H., Hildebrandt, L., Hillamo, R., Jimenez, J. L., Laaksonen, A., McFiggans, G., Mohr, C., O'Dowd, C., Otjes, R., Ovadnevaite, J., Pandis, S. N., Poulain, L., Schlag, P., Sellegri, K., Swietlicki, E., Tiitta, P., Vermeulen, A., Wahner, A., Worsnop, D., and Wu, H.-C.: Ubiquity of organic nitrates from nighttime chemistry in the European submicron aerosol, Geophys. Res. Lett., 43, 7735–7744, https://doi.org/10.1002/2016GL069239, 2016.

Kraus, S.: DOASIS – A framework design for DOAS, PhD thesis, University of Heidelberg, Heidelberg, Germany, ISBN: 978-3-8322-5452-0, 2006.

Kumar, V., Slowik, J. G., Baltensperger, U., Prevot, A. S. H., and Bell, D. M.: Time-Resolved Molecular Characterization of Secondary Organic Aerosol Formed from OH and NO_3 Radical Initiated Oxidation of a Mixture of Aromatic Precursors, Environ. Sci. Technol., 57, 11572–11582, https://doi.org/10.1021/acs.est.3c00225, 2023.

Langridge, J. M., Ball, S. M., Shillings, A. J. L., and Jones, R. L.: A broadband absorption spectrometer using light emitting diodes for ultrasensitive, in situ trace gas detection, Rev. Sci. Instrum., 79, 123110, https://doi.org/10.1063/1.3046282, 2008.

Lee, B. H., Mohr, C., Lopez-Hilfiker, F. D., Lutz, A., Hallquist, M., Lee, L., Romer, P., Cohen, R. C., Iyer, S., Kurtén, T., Hu, W., Day, D. A., Campuzano-Jost, P., Jimenez, J. L., Xu, L., Ng, N. L., Guo, H., Weber, R. J., Wild, R. J., Brown, S. S., Koss, A., de Gouw, J., Olson, K., Goldstein, A. H., Seco, R., Kim, S., McAvey, K., Shepson, P. B., Starn, T., Baumann, K., Edgerton, E. S., Liu, J., Shilling, J. E., Miller, D. O., Brune, W., Schobesberger, S., D'Ambro, E. L., and Thornton, J. A.: Highly functionalized organic nitrates in the southeast United States: Contribution to secondary organic aerosol and reactive nitrogen budgets, Proc. Natl. Acad. Sci., 113, 1516–1521, https://doi.org/10.1073/pnas.1508108113, 2016.

Lelieveld, J., Pozzer, A., Poschl, U., Fnais, M., Haines, A., and Munzel, T.: Loss of life expectancy from air pollution compared to other risk factors: a worldwide perspective, Cardiovasc. Res., 116, 1334–1334, https://doi.org/10.1093/cvr/cvaa073, 2020.

Leser, H., Honninger, G., and Platt, U.: MAX-DOAS measurements of BrO and NO_2 in the marine boundary layer, Geophys. Res. Lett., 30, https://doi.org/10.1029/2002GL015811, 2003.

Li, Z., Hu, R., Xie, P., Chen, H., Wu, S., Wang, F., Wang, Y., Ling, L., Liu, J., and Liu, W.: Development of a portable cavity ring down spectroscopy instrument for simultaneous, in situ measurement of NO_3 and N_2O_5, Opt. Express, 26, A433–A449, https://doi.org/10.1364/OE.26.00A433, 2018.

Liebmann, J., Karu, E., Sobanski, N., Schuladen, J., Ehn, M., Schallhart, S., Quéléver, L., Hellen, H., Hakola, H., Hoffmann, T., Williams, J., Fischer, H., Lelieveld, J., and Crowley, J. N.: Direct measurement of NO_3 radical reactivity in a boreal forest, Atmos. Chem. Phys., 18, 3799–3815, https://doi.org/10.5194/acp-18-3799-2018, 2018.

Liebmann, J., Sobanski, N., Schuladen, J., Karu, E., Hellén, H., Hakola, H., Zha, Q., Ehn, M., Riva, M., Heikkinen, L., Williams, J., Fischer, H., Lelieveld, J., and Crowley, J. N.: Alkyl nitrates in the boreal forest: formation via the NO_3-, OH- and O_3-induced oxidation of biogenic volatile organic compounds and ambient lifetimes, Atmos. Chem. Phys., 19, 10391–10403, https://doi.org/10.5194/acp-19-10391-2019, 2019.

Lin, C., Hu, R., Xie, P., Lou, S., Zhang, G., Tong, J., Liu, J., and Liu, W.: Nocturnal atmospheric chemistry of NO_3 and N_2O_5 over Changzhou in the Yangtze River Delta in China, Atmos. Chem. Complex Air Pollut., 114, 376–390, https://doi.org/10.1016/j.jes.2021.09.016, 2022.

Lin, Y., Xia, H., Sun, P., Du, S., Liu, Y., Wu, B., Pang, T., and Zhang, Z.: Development and applications of high sensitivity cavity ring-down spectroscopy: a review, Infrared Phys. Technol., 156, 106626, https://doi.org/10.1016/j.infrared.2026.106626, 2026.

Ling, L., Li, W., and Zhang, Q.: A pptv Level Incoherent Broadband Cavity-Enhanced Absorption Spectrometer for the Measurement of Atmospheric NO_3, Atmosphere, 14, 543, https://doi.org/10.3390/atmos14030543, 2023.

Logan, J. A.: Nitrogen oxides in the troposphere: Global and regional budgets, J. Geophys. Res. Oceans, 88, 10785–10807, https://doi.org/10.1029/JC088iC15p10785, 1983.

Matsumoto, J., Kosugi, N., Imai, H., and Kajii, Y.: Development of a measurement system for nitrate radical and dinitrogen pentoxide using a thermal conversion/laser-induced fluorescence technique, Rev. Sci. Instrum., 76, 064101, https://doi.org/10.1063/1.1927098, 2005.

McKay, M. D., Beckman, R. J., and Conover, W. J.: A Comparison of Three Methods for Selecting Values of Input Variables in the Analysis of Output from a Computer Code, Technometrics, 21, 239–245, https://doi.org/10.2307/1268522, 1979.

McLaren, R., Salmon, R. A., Liggio, J., Hayden, K. L., Anlauf, K. G., and Leaitch, W. R.: Nighttime chemistry at a rural site in the Lower Fraser Valley, Atmos. Environ., 38, 5837–5848, https://doi.org/10.1016/j.atmosenv.2004.03.074, 2004.

Mermet, K., Perraudin, E., Dusanter, S., Sauvage, S., Léonardis, T., Flaud, P.-M., Bsaibes, S., Kammer, J., Michoud, V., Gratien, A., Cirtog, M., Al Ajami, M., Truong, F., Batut, S., Hecquet, C., Doussin, J.-F., Schoemaecker, C., Gros, V., Locoge, N., and Villenave, E.: Atmospheric reactivity of biogenic volatile organic compounds in a maritime pine forest during the LANDEX episode 1 field campaign, Sci. Total Environ., 756, 144129, https://doi.org/10.1016/j.scitotenv.2020.144129, 2021.

Merten, A., Tschritter, J., and Platt, U.: Design of differential optical absorption spectroscopy long-path telescopes based on fiber optics, Appl. Opt., 50, 738–754, https://doi.org/10.1364/AO.50.000738, 2011.

Mogensen, D., Gierens, R., Crowley, J. N., Keronen, P., Smolander, S., Sogachev, A., Nölscher, A. C., Zhou, L., Kulmala, M., Tang, M. J., Williams, J., and Boy, M.: Simulations of atmospheric OH, O_3 and NO_3 reactivities within and above the boreal forest, Atmos. Chem. Phys., 15, 3909–3932, https://doi.org/10.5194/acp-15-3909-2015, 2015.

Monks, P. S.: Gas-phase radical chemistry in the troposphere, Chem. Soc. Rev., 34, 376–395, https://doi.org/10.1039/B307982C, 2005.

Nam, W., Cho, C., Perdigones, B., Rhee, T. S., and Min, K.-E.: Development of a broadband cavity-enhanced absorption spectrometer for simultaneous measurements of ambient NO_3, NO_2, and H_2O, Atmos. Meas. Tech., 15, 4473–4487, https://doi.org/10.5194/amt-15-4473-2022, 2022.

Ng, N. L., Brown, S. S., Archibald, A. T., Atlas, E., Cohen, R. C., Crowley, J. N., Day, D. A., Donahue, N. M., Fry, J. L., Fuchs, H., Griffin, R. J., Guzman, M. I., Herrmann, H., Hodzic, A., Iinuma, Y., Jimenez, J. L., Kiendler-Scharr, A., Lee, B. H., Luecken, D. J., Mao, J., McLaren, R., Mutzel, A., Osthoff, H. D., Ouyang, B., Picquet-Varrault, B., Platt, U., Pye, H. O. T., Rudich, Y., Schwantes, R. H., Shiraiwa, M., Stutz, J., Thornton, J. A., Tilgner, A., Williams, B. J., and Zaveri, R. A.: Nitrate radicals and biogenic volatile organic compounds: oxidation, mechanisms, and organic aerosol, Atmos. Chem. Phys., 17, 2103–2162, https://doi.org/10.5194/acp-17-2103-2017, 2017.

Nussbaumer, C. M., Parchatka, U., Tadic, I., Bohn, B., Marno, D., Martinez, M., Rohloff, R., Harder, H., Kluge, F., Pfeilsticker, K., Obersteiner, F., Zoger, M., Doerich, R., Crowley, J. N., Lelieveld, J., and Fischer, H.: Modification of a conventional photolytic converter for improving aircraft measurements of NO_2 via chemiluminescence, Atmos. Meas. Tech., 14, 6759–6776, https://doi.org/10.5194/amt-14-6759-2021, 2021.

Odame-Ankrah, C. A. and Osthoff, H. D.: A Compact Diode Laser Cavity Ring-Down Spectrometer for Atmospheric Measurements of NO_3 and N_2O_5 with Automated Zeroing and Calibration, Appl. Spectrosc., 65, 1260–1268, https://doi.org/10.1366/11-06384, 2011.

Ohara, N., Shioji, T., Matsumoto, J., Inomata, S., Sakamoto, Y., Kajii, Y., Shiigi, H., and Sadanaga, Y.: Improved continuous measurement system for atmospheric total peroxy and total organic nitrate under the high NO_x condition, Rev. Sci. Instrum., 95, 045101, https://doi.org/10.1063/5.0172219, 2024.

Orphal, J., Fellows, C. E., and Flaud, P. M.: The visible absorption spectrum of NO_3 measured by high-resolution Fourier transform spectroscopy, J. Geophys. Res.-Atmos., 108, 4077, https://doi.org/10.1029/2002JD002489, 2003.

Osthoff, H. D., Pilling, M. J., Ravishankara, A. R., and Brown, S. S.: Temperature dependence of the NO_3 absorption cross-section above 298 K and determination of the equilibrium constant for $NO_3 + NO_2 \rightleftharpoons N_2O_5$ at atmospherically relevant conditions, Phys. Chem. Chem. Phys., 9, 5785–5793, https://doi.org/10.1039/b709193a, 2007.

Pandey Deolal, S., Brunner, D., Steinbacher, M., Weers, U., and Staehelin, J.: Long-term in situ measurements of NO_x and NO_y at Jungfraujoch 1998–2009: time series analysis and evaluation, Atmos Chem Phys, 12, 2551–2566, https://doi.org/10.5194/acp-12-2551-2012, 2012.

Parrish, D. D., Buhr, M. P., Trainer, M., Norton, R. B., Shimshock, J. P., Fehsenfeld, F. C., Anlauf, K. G., Bottenheim, J. W., Tang, Y. Z., Wiebe, H. A., Roberts, J. M., Tanner, R. L., Newman, L., Bowersox, V. C., Olszyna, K. J., Bailey, E. M., Rodgers, M. O., Wang, T., Berresheim, H., Roychowdhury, U. K., and Demerjiani, K. L.: The total reactive oxidized nitrogen levels and the partitioning between the individual species at six rural sites in eastern North America, J. Geophys. Res. Atmos., 98, 2927–2939, https://doi.org/10.1029/92JD02384, 1993.

Paul, D., Furgeson, A., and Osthoff, H. D.: Measurements of total peroxy and alkyl nitrate abundances in laboratory-generated gas samples by thermal dissociation cavity ring-down spectroscopy, Rev. Sci. Instrum., 80, 114101, https://doi.org/10.1063/1.3258204, 2009.

Phillips, G. J., Thieser, J., Tang, M. J., Sobanski, N., Schuster, G., Fachinger, J., Drewnick, F., Borrmann, S., Bingemer, H., Lelieveld, J., and Crowley, J. N.: Estimating N_2O_5 uptake coefficients using ambient measurements of NO_3, N_2O_5, $ClNO_2$ and particle-phase nitrate, Atmos. Chem. Phys/, 16, 13231–13249, https://doi.org/10.5194/acp-16-13231-2016, 2016.

Platt, U. and Stutz, J.: The Design of DOAS Instruments, in: Differential Optical Absorption Spectroscopy: Principles and Applications, edited by: Platt, U. and Stutz, J., Springer Berlin Heidelberg, Berlin, Heidelberg, 175–285, https://doi.org/10.1007/978-3-540-75776-4_7, 2008.

Platt, U., Perner, D., Winer, A. M., Harris, G. W., and Pitts, J. N. J.: Detection of NO_3 in the polluted troposphere by differential optical absorption, Geophys. Res. Lett., 7, 89–92, https://doi.org/10.1029/GL007i001p00089, 1980.

Platt, U., Perner, D., Schröder, J., Kessler, C., and Toennissen, A.: The diurnal variation of NO_3, J. Geophys. Res., 86, 11965–11970, https://doi.org/10.1029/JC086iC12p11965, 1981.

Pye, H. O. T., Chan, A. W. H., Barkley, M. P., and Seinfeld, J. H.: Global modeling of organic aerosol: the importance of reactive nitrogen (NO_x and NO_3), Atmos. Chem. Phys., 10, 11261–11276, https://doi.org/10.5194/acp-10-11261-2010, 2010.

Pye, H. O. T., Luecken, D. J., Xu, L., Boyd, C. M., Ng, N. L., Baker, K. R., Ayres, B. R., Bash, J. O., Baumann, K., Carter, W. P. L., Edgerton, E., Fry, J. L., Hutzell, W. T., Schwede, D. B., and Shepson, P. B.: Modeling the Current and Future Roles of Particulate Organic Nitrates in the Southeastern United States, Environ. Sci. Technol., 49, 14195–14203, https://doi.org/10.1021/acs.est.5b03738, 2015.

Reed, C., Evans, M. J., Di Carlo, P., Lee, J. D., and Carpenter, L. J.: Interferences in photolytic NO_2 measurements: explanation for an apparent missing oxidant?, Atmos. Chem. Phys., 16, 4707–4724, https://doi.org/10.5194/acp-16-4707-2016, 2016.

Rindelaub, J. D., McAvey, K. M., and Shepson, P. B.: The photochemical production of organic nitrates from α-pinene and loss via acid-dependent particle phase hydrolysis, Atmos. Environ., 100, 193–201, https://doi.org/10.1016/j.atmosenv.2014.11.010, 2015.

Schueneman, M. K., Day, D. A., Jenks, O. J., Kim, D., Handschy, A., Morris, M. A., de Gouw, J. A., Decker, Z. C. J., Ziemann, P. J., and Jimenez, J. L.: Secondary Organic Aerosol Yields from NO_3 Oxidation of Phenolic, Aromatic, and Heterocyclic

VOCs: Implications for Biomass Burning Plumes, Envrion. Sci. Technol. Air, 2, 2342–2352, https://doi.org/10.1021/acsestair.4c00332, 2025.

Schuster, G., Labazan, I., and Crowley, J. N.: A cavity ring down / cavity enhanced absorption device for measurement of ambient NO_3 and N_2O_5, Atmos. Meas. Tech., 2, 1–13, https://doi.org/10.5194/amt-2-1-2009, 2009.

Seinfeld, J. H. and Pandis, S. N.: Atmospheric Chemistry and Physics: From Air Pollution to Climate Change, Wiley, ISBN: 978-1-119-22117-3, 2012.

Slusher, D. L., Huey, L. G., Tanner, D. J., Flocke, F. M., and Roberts, J. M.: A thermal dissociation-chemical ionization mass spectrometry (TD-CIMS) technique for the simultaneous measurement of peroxyacyl nitrates and dinitrogen pentoxide, J. Geophys. Res.-Atmos., 109, D19315, https://doi.org/10.1029/2004JD004670, 2004.

Sobanski, N., Schuladen, J., Schuster, G., Lelieveld, J., and Crowley, J. N.: A five-channel cavity ring-down spectrometer for the detection of NO_2, NO_3, N_2O_5, total peroxy nitrates and total alkyl nitrates, Atmos. Meas. Tech., 9, 5103–5118, https://doi.org/10.5194/amt-9-5103-2016, 2016.

Sommariva, R., Pilling, M. J., Bloss, W. J., Heard, D. E., Lee, J. D., Fleming, Z. L., Monks, P. S., Plane, J. M. C., Saiz-Lopez, A., Ball, S. M., Bitter, M., Jones, R. L., Brough, N., Penkett, S. A., Hopkins, J. R., Lewis, A. C., and Read, K. A.: Night-time radical chemistry during the NAMBLEX campaign, Atmos. Chem. Phys., 7, 587–598, https://doi.org/10.5194/acp-7-587-2007, 2007.

Storn, R. and Price, K.: Differential Evolution – A Simple and Efficient Heuristic for global Optimization over Continuous Spaces, J. Glob. Optim., 11, 341–359, https://doi.org/10.1023/A:1008202821328, 1997.

Stratmann, G., Ziereis, H., Stock, P., Brenninkmeijer, C. A. M., Zahn, A., Rauthe-Schöch, A., Velthoven, P. V., Schlager, H., and Volz-Thomas, A.: NO and NOy in the upper troposphere: Nine years of CARIBIC measurements onboard a passenger aircraft, Atmos. Environ., 133, 93–111, https://doi.org/10.1016/j.atmosenv.2016.02.035, 2016.

Suhail, K., George, M., Chandran, S., Varma, R., Venables, D. S., Wang, M., and Chen, J.: Open path incoherent broadband cavity-enhanced measurements of NO_3 radical and aerosol extinction in the North China Plain, Spectrochim. Acta. A. Mol. Biomol. Spectrosc., 208, 24–31, https://doi.org/10.1016/j.saa.2018.09.023, 2019.

Tadic, I., Crowley, J. N., Dienhart, D., Eger, P., Harder, H., Hottmann, B., Martinez, M., Parchatka, U., Paris, J. D., Pozzer, A., Rohloff, R., Schuladen, J., Shenolikar, J., Tauer, S., Lelieveld, J., and Fischer, H.: Net ozone production and its relationship to nitrogen oxides and volatile organic compounds in the marine boundary layer around the Arabian Peninsula, Atmos. Chem. Phys., 20, 6769–6787, https://doi.org/10.5194/acp-20-6769-2020, 2020.

Thieser, J., Schuster, G., Phillips, G. J., Reiffs, A., Parchatka, U., Pöhler, D., Lelieveld, J., and Crowley, J. N.: A two-channel, thermal dissociation cavity-ringdown spectrometer for the detection of ambient NO_2, RO_2NO_2 and $RONO_2$, Atmos. Meas. Tech., 9, 553–576, https://doi.org/10.5194/amt-9-553-2016, 2016.

Türk, G. N. T. E., Andersen, S. T., Dewald, P., Schuladen, J., Lelieveld, J., and Crowley, J. N.: A small-footprint Cavity Ring-Down Spectroscopy instrument for in situ measurements of NO_3 and N_2O_5, Atmos. Meas. Tech., 19, 4815–4832, https://doi.org/10.5194/amt-19-4815-2026, 2026.

Vandaele, A. C., Hermans, C., Simon, P. C., Carleer, M., Colin, R., Fally, S., Merienne, M. F., Jenouvrier, A., and Coquart, B.: Measurements of the NO_2 absorption cross-section from 42 000 cm^{-1} to 10 000 cm^{-1} (238-1000 nm) at 220 K and 294 K, J. Quant. Spectrosc. Radiat. Transf., 59, 171–184, https://doi.org/10.1016/S0022-4073(97)00168-4, 1998.

Varma, R. M., Venables, D. S., Ruth, A. A., Heitmann, U., Schlosser, E., and Dixneuf, S.: Long optical cavities for open-path monitoring of atmospheric trace gases and aerosol extinction, Appl. Opt., 48, B159–B171, https://doi.org/10.1364/AO.48.00B159, 2009.

Varma, R. M., Ball, S. M., Brauers, T., Dorn, H.-P., Heitmann, U., Jones, R. L., Platt, U., Pöhler, D., Ruth, A. A., Shillings, A. J. L., Thieser, J., Wahner, A., and Venables, D. S.: Light extinction by secondary organic aerosol: an intercomparison of three broadband cavity spectrometers, Atmos. Meas. Tech., 6, 3115–3130, https://doi.org/10.5194/amt-6-3115-2013, 2013.

Vaughan, S., Gherman, T., Ruth, A. A., and Orphal, J.: Incoherent broad-band cavity-enhanced absorption spectroscopy of the marine boundary layer species I_2, IO and OIO, Phys. Chem. Chem. Phys., 10, 4471–4477, https://doi.org/10.1039/b802618a, 2008.

Venables, D. S., Gherman, T., Orphal, J., Wenger, J. C., and Ruth, A. A.: High sensitivity in situ monitoring of NO_3 in an atmospheric simulation chamber using incoherent broadband cavity-enhanced absorption spectroscopy, Environ. Sci. Technol., 40, 6758–6763, https://doi.org/10.1021/es061076j, 2006.

Ventrillard-Courtillot, I., Sciamma O'Brien, E., Kassi, S., Méjean, G., and Romanini, D.: Incoherent broad-band cavity-enhanced absorption spectroscopy for simultaneous trace measurements of NO_2 and NO_3 with a LED source, Appl. Phys. B, 101, 661–669, https://doi.org/10.1007/s00340-010-4253-x, 2010.

Virtanen, P., Gommers, R., Oliphant, T. E., Haberland, M., Reddy, T., Cournapeau, D., Burovski, E., Peterson, P., Weckesser, W., Bright, J., van der Walt, S. J., Brett, M., Wilson, J., Millman, K. J., Mayorov, N., Nelson, A. R. J., Jones, E., Kern, R., Larson, E., Carey, C. J., Polat, İ., Feng, Y., Moore, E. W., VanderPlas, J., Laxalde, D., Perktold, J., Cimrman, R., Henriksen, I., Quintero, E. A., Harris, C. R., Archibald, A. M., Ribeiro, A. H., Pedregosa, F., van Mulbregt, P., Vijaykumar, A., Bardelli, A. P., Rothberg, A., Hilboll, A., Kloeckner, A., Scopatz, A., Lee, A., Rokem, A., Woods, C. N., Fulton, C., Masson, C., Häggström, C., Fitzgerald, C., Nicholson, D. A., Hagen, D. R., Pasechnik, D. V., Olivetti, E., Martin, E., Wieser, E., Silva, F., Lenders, F., Wilhelm, F., Young, G., Price, G. A., Ingold, G.-L., Allen, G. E., Lee, G. R., Audren, H., Probst, I., Dietrich, J. P., Silterra, J., Webber, J. T., Slavič, J., Nothman, J., Buchner, J., Kulick, J., Schönberger, J. L., de Miranda Cardoso, J. V., Reimer, J., Harrington, J., Rodríguez, J. L. C., Nunez-Iglesias, J., Kuczynski, J., Tritz, K., Thoma, M., Newville, M., Kümmerer, M., Bolingbroke, M., Tartre, M., Pak, M., Smith, N. J., Nowaczyk, N., Shebanov, N., Pavlyk, O., Brodtkorb, P. A., Lee, P., McGibbon, R. T., Feldbauer, R., Lewis, S., Tygier, S., Sievert, S., Vigna, S., Peterson, S., More, S., Pudlik, T., et al.: SciPy 1.0: fundamental algorithms for scientific computing in Python, Nat. Methods, 17, 261–272, https://doi.org/10.1038/s41592-019-0686-2, 2020.

Vrekoussis, M., Mihalopoulos, N., Gerasopoulos, E., Kanakidou, M., Crutzen, P. J., and Lelieveld, J.: Two-years of NO_3 radical observations in the boundary layer over the Eastern Mediterranean, Atmos. Chem. Phys., 7, 315–327, https://doi.org/10.5194/acp-7-315-2007, 2007.

Wagner, N. L., Dube, W. P., Washenfelder, R. A., Young, C. J., Pollack, I. B., Ryerson, T. B., and Brown, S. S.: Diode laser-based cavity ring-down instrument for NO_3, N_2O_5, NO, NO_2 and O_3 from aircraft, Atmos. Meas. Tech., 4, 1227–1240, https://doi.org/10.5194/amt-4-1227-2011, 2011.

Wang, D., Hu, R., Xie, P., Liu, J., Liu, W., Qin, M., Ling, L., Zeng, Y., Chen, H., Xing, X., Zhu, G., Wu, J., Duan, J., Lu, X., and Shen, L.: Diode laser cavity ring-down spectroscopy for in situ measurement of NO_3 radical in ambient air, J. Quant. Spectrosc. Radiat. Transf., 166, 23–29, https://doi.org/10.1016/j.jqsrt.2015.07.005, 2015.

Wang, H. and Lu, K.: Monitoring Ambient Nitrate Radical by Open-Path Cavity-Enhanced Absorption Spectroscopy, Anal. Chem., 91, 10687–10693, https://doi.org/10.1021/acs.analchem.9b01971, 2019.

Wang, H., Chen, J., and Lu, K.: Development of a portable cavity-enhanced absorption spectrometer for the measurement of ambient NO_3 and N_2O_5: experimental setup, lab characterizations, and field applications in a polluted urban environment, Atmos. Meas. Tech., 10, 1465–1479, https://doi.org/10.5194/amt-10-1465-2017, 2017.

Wang, J., Doussin, J. F., Perrier, S., Perraudin, E., Katrib, Y., Pangui, E., and Picquet-Varrault, B.: Design of a new multi-phase experimental simulation chamber for atmospheric photosmog, aerosol and cloud chemistry research, Atmos. Meas. Tech., 4, 2465–2494, https://doi.org/10.5194/amt-4-2465-2011, 2011.

Wang, M., Lou, S., Hu, W., Wang, H., Wang, X., Fan, F., Varma, R., Venables, D. S., and Chen, J.: Intercomparison of NO_3 under Humid Conditions with Open-Path and Extractive IBBCEAS in an Atmospheric Reaction Chamber, Remote Sens., 15, 739, https://doi.org/10.3390/rs15030739, 2023.

Wayne, R. P., Barnes, I., Biggs, P., Burrows, J. P., Canosamas, C. E., Hjorth, J., Lebras, G., Moortgat, G. K., Perner, D., Poulet, G., Restelli, G., and Sidebottom, H.: The Nitrate Radical - Physics, Chemistry, and the Atmosphere, Atmos. Environ., 25, 1–203, https://doi.org/10.1016/0960-1686(91)90192-A, 1991.

Wennberg, P. O., Bates, K. H., Crounse, J. D., Dodson, L. G., McVay, R. C., Mertens, L. A., Nguyen, T. B., Praske, E., Schwantes, R. H., Smarte, M. D., St Clair, J. M., Teng, A. P., Zhang, X., and Seinfeld, J. H.: Gas-Phase Reactions of Isoprene and Its Major Oxidation Products, Chem. Rev., 118, 3337–3390, https://doi.org/10.1021/acs.chemrev.7b00439, 2018.

Wild, R. J., Edwards, P. M., Dube, W. P., Baumann, K., Edgerton, E. S., Quinn, P. K., Roberts, J. M., Rollins, A. W., Veres, P. R., Warneke, C., Williams, E. J., Yuan, B., and Brown, S. S.: A measurement of total reactive nitrogen, NO_y, together with NO_2, NO, and O_3 via cavity ring-down spectroscopy, Environ. Sci. Technol., 48, 9609–9615, https://doi.org/doi:10.1021/es501896w, 2014.

Wild, R. J., Edwards, P. M., Bates, T. S., Cohen, R. C., de Gouw, J. A., Dube, W. P., Gilman, J. B., Holloway, J., Kercher, J., Koss, A. R., Lee, L., Lerner, B. M., McLaren, R., Quinn, P. K., Roberts, J. M., Stutz, J., Thornton, J. A., Veres, P. R., Warneke, C., Williams, E., Young, C. J., Yuan, B., Zarzana, K. J., and Brown, S. S.: Reactive nitrogen partitioning and its relationship to winter ozone events in Utah, Atmos. Chem. Phys., 16, 573–583, https://doi.org/10.5194/acp-16-573-2016, 2016.

Williams, E. J., Baumann, K., Roberts, J. M., Bertman, S. B., Norton, R. B., Fehsenfeld, F. C., Springston, S. R., Nunnermacker, L. J., Newman, L., Olszyna, K., Meagher, J., Hartsell, B., Edgerton, E., Pearson, J. R., and Rodgers, M. O.: Intercomparison of ground-based NO_y measurement techniques, J. Geophys. Res. Atmos., 103, 22261–22280, https://doi.org/10.1029/98JD00074, 1998.

Womack, C. C., Neuman, J. A., Veres, P. R., Eilerman, S. J., Brock, C. A., Decker, Z. C. J., Zarzana, K. J., Dube, W. P., Wild, R. J., Wooldridge, P. J., Cohen, R. C., and Brown, S. S.: Evaluation of the accuracy of thermal dissociation CRDS and LIF techniques for atmospheric measurement of reactive nitrogen species, Atmos. Meas. Tech., 10, 1911–1926, https://doi.org/10.5194/amt-10-1911-2017, 2017.

Wood, E. C., Wooldridge, P. J., Freese, J. H., Albrecht, T., and Cohen, R. C.: Prototype for In Situ Detection of Atmospheric NO_3 and N_2O_5 via Laser-Induced Fluorescence, Environ. Sci. Technol., 37, 5732–5738, https://doi.org/10.1021/es034507w, 2003.

Wu, H., Chen, J., Liu, A., Hu, S., and Zhang, J.: Cavity ring-down spectroscopy measurements of ambient NO_3 and N_2O_5, Chin. J. Chem. Phys., 33, 1–7, https://doi.org/10.1063/1674-0068/cjcp1910173, 2020.

Wüst, L., Dewald, P., Türk, G. N. T. E., Lelieveld, J., and Crowley, J. N.: Influence of ambient NO and NO_2 on the quantification of total peroxy nitrates (ΣPNs) and total alkyl nitrates (ΣANs) by thermal dissociation cavity ring-down spectroscopy (TD-CRDS), Atmos. Meas. Tech., 18, 1943–1959, https://doi.org/10.5194/amt-18-1943-2025, 2025.

Yáñez-Serrano, A. M., Nölscher, A. C., Bourtsoukidis, E., Gomes Alves, E., Ganzeveld, L., Bonn, B., Wolff, S., Sa, M., Yamasoe, M., Williams, J., Andreae, M. O., and Kesselmeier, J.: Monoterpene chemical speciation in a tropical rainforest: variation with season, height, and time of day at the Amazon Tall Tower Observatory (ATTO), Atmos. Chem. Phys., 18, 3403–3418, https://doi.org/10.5194/acp-18-3403-2018, 2018.

Zhang, X., Liu, H., Cheng, J., Song, W., Wang, H., Zhang, Y., and Wang, X.: Gas-Phase Oxidation of Guaiacol by NO_3 Radicals: Kinetic Measurements and Implications, Environ. Sci. Technol. Air, 2, 903–910, https://doi.org/10.1021/acsestair.4c00353, 2025.

Figures

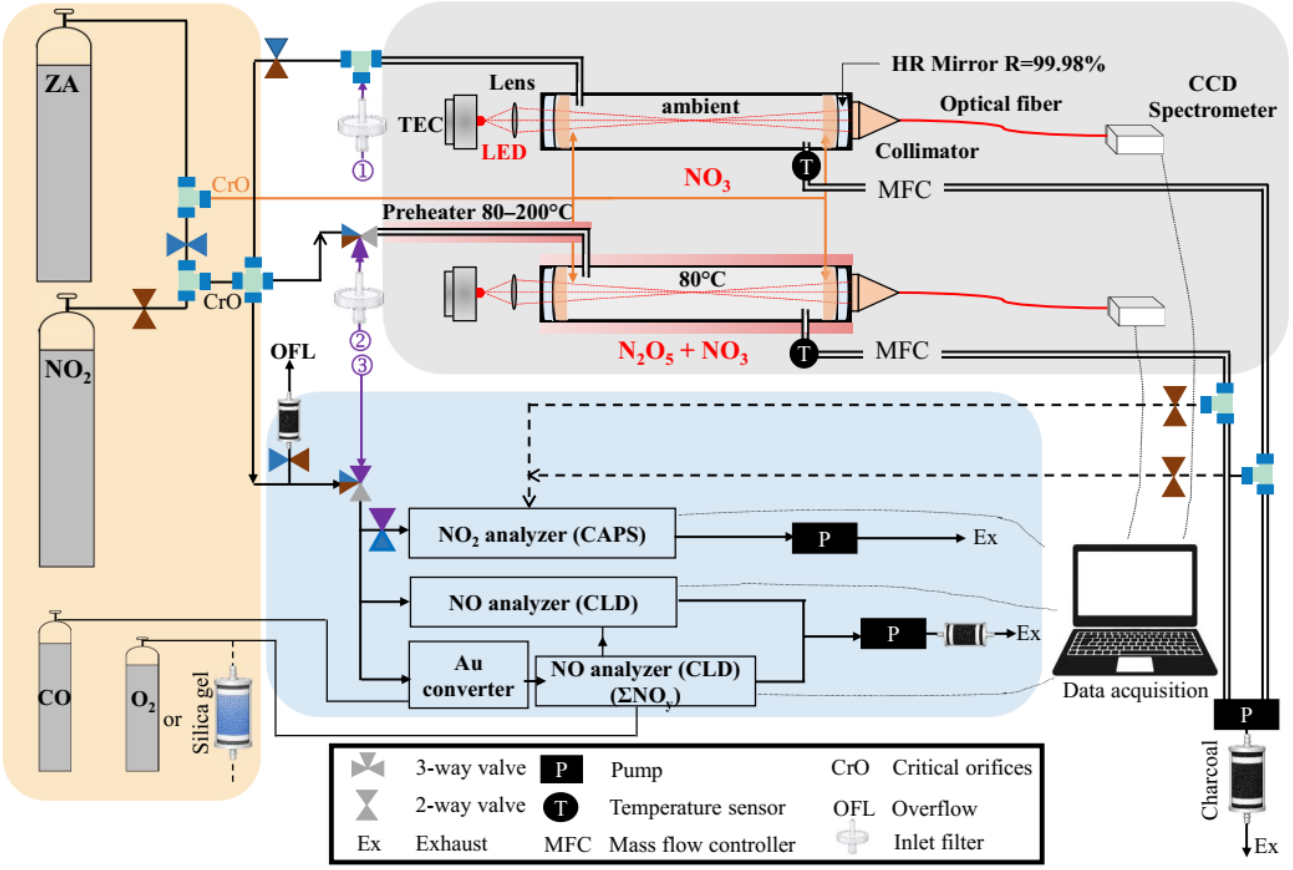


Figure 1. Schematic diagram of the NOyBOx instrument. The two custom-built IBBCEAS subsystems with separate inlets 1 and 2 is shaded grey. The commercial analyzer subsystem for NO, NO_2, and total gas-phase NO_y is shaded blue and share inlet 3. The gas supply assembly for purging (orange solid lines), background and calibration measurements is marked in orange. The valves are coloured according to the modes (blue: background, brown: calibration, purple: sampling, grey: always open) they are active in. The black dashed lines show how the cavity exhaust flow is coupled to the NO_2 analyser during calibration periods. Note that the NO_3 channel's inlet is equipped with an additional charcoal filter (not shown) when calibrated with NO_2.

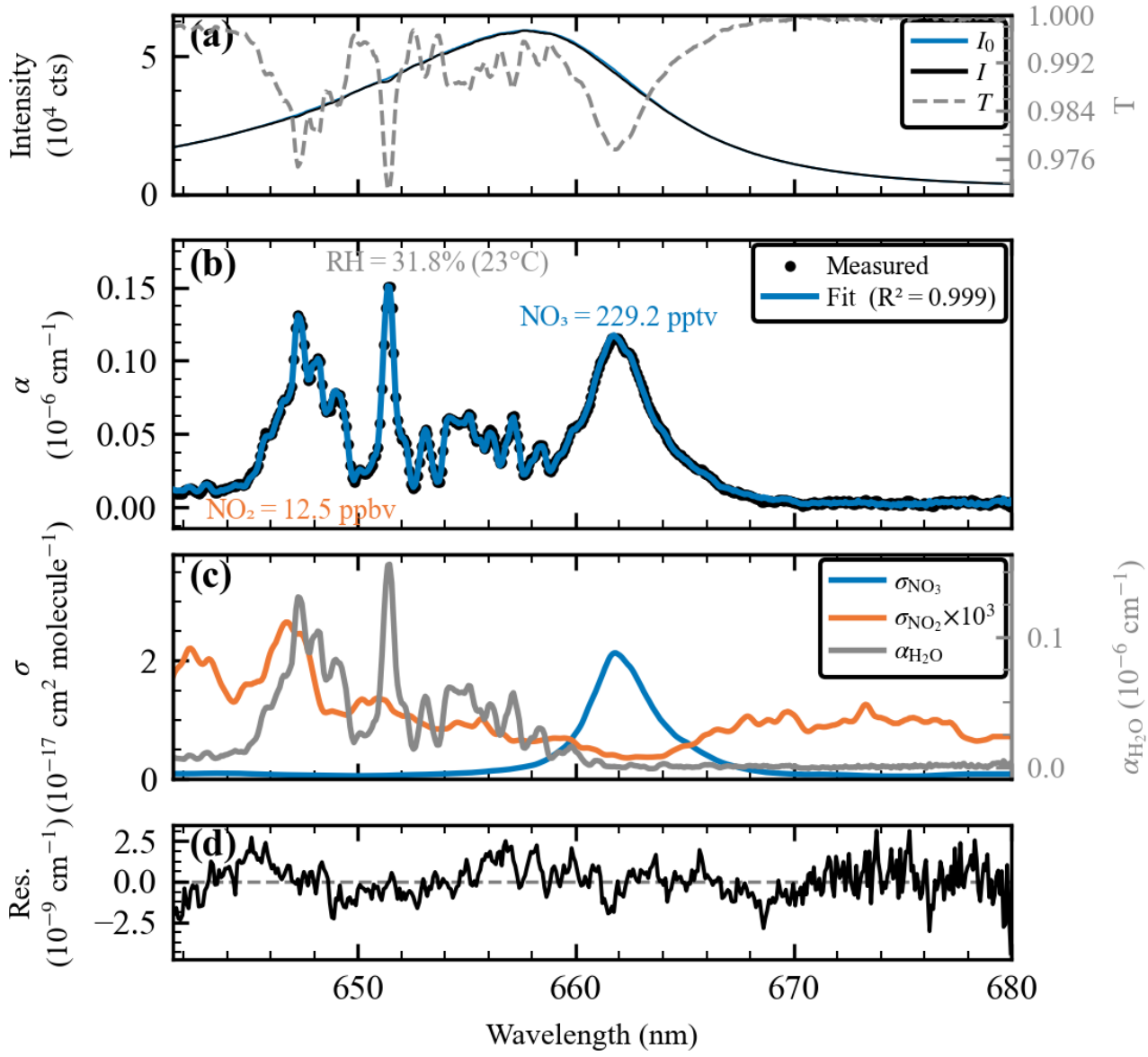


Figure 2. Exemplary IBBCEAS spectral retrieval for a representative measurement at the simulation chamber CESAM with the NO_3 channel: (a) Raw spectra I_0 (reference, blue) and I (sample, black) with the corresponding transmission $T = I/I_0$ on the right axis (grey dashed). (b) Measured effective absorption coefficient α (black dots) and best-fit model (blue line); retrieved concentrations are annotated. (c) Reference absorption cross-sections of NO_3 (blue, Orphal et al., 2003) and NO_2 $\times 10^3$ (orange, Vandaele et al., 1998) convolved with the instrument spectral response function on the left axis, and the effective H_2O absorption coefficient $\boldsymbol{\alpha_{H_2O}}$ (RH = 33 %, 23 °C) on the right axis (grey). (d) Fit residual (black solid line).

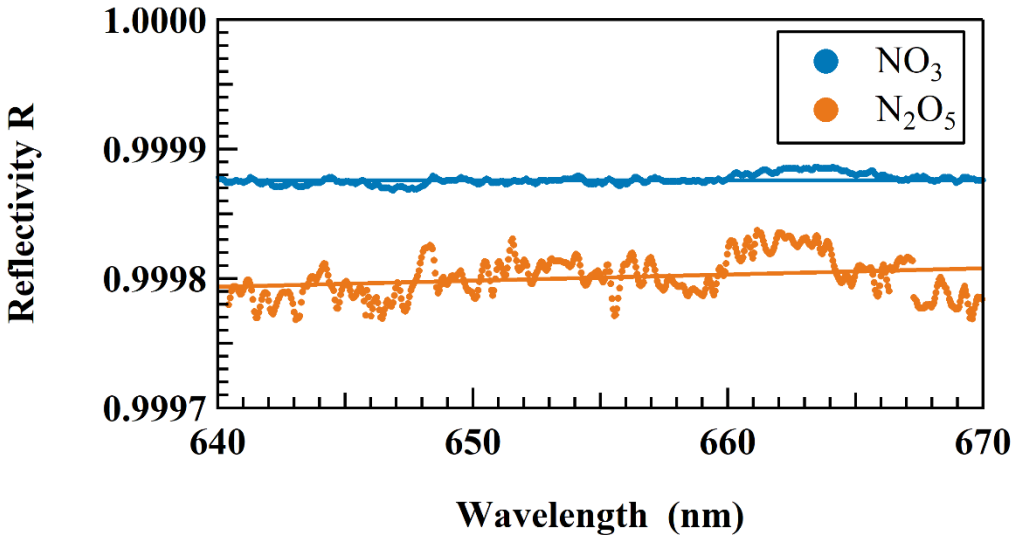


Figure 3. Exemplary mirror reflectivity measurements for the NO_3 (blue circles) and N_2O_5 (orange circles) channels along with linear regressions (same coloured solid lines).

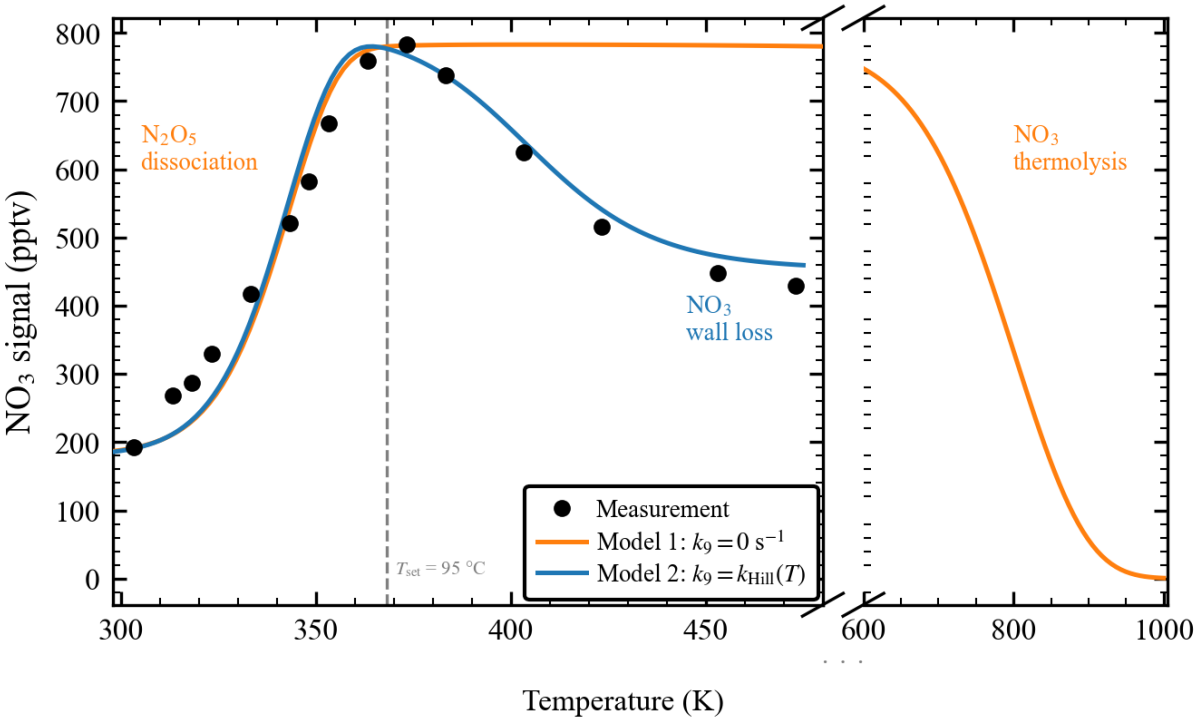


Figure 4. NO_3 equivalents detected in the unheated N_2O_5 cavity (black points) resulting from NO_3 and thermally dissociated N_2O_5 provided from the glass reactor as a function of the preheater temperature setpoint ("thermogram"). Model 1 (orange line) shows the theoretically expected thermogram between 300 and 1000 K using IUPAC-recommended reaction rate coefficients for k_2 and k_3 as well as k_8 according to Womack et al. (2017). Model 2 includes a temperature-dependent NO_3 wall loss rate (k_{Hill} (T / s^{-1}) = 0.1 s^{-1} + (0.3 x T^{25} / (410^{25} + T^{25})) and was adjusted to reproduce the observations. The vertical grey dashed line indicates the optimal temperature setpoint of 95 °C.

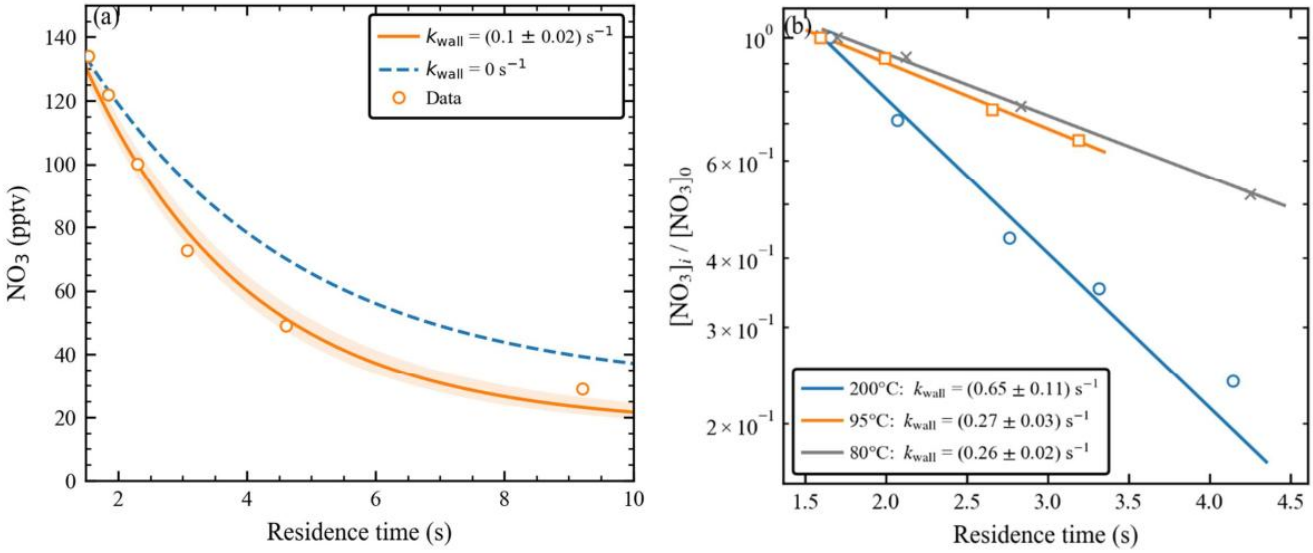


Figure 5. (a) Dependency between residence time and measured NO_3 mixing ratios (orange circles) in the NO_3 cavity. The blue dashed line indicates modelled NO_3 mixing ratios accounting for reestablishment of the thermal equilibrium while the solid orange line shows a model run including an NO_3 wall loss rate adjusted to reproduce observations. (b) Dependency between measured NO_3 mixing ratios and the summed residence time in N_2O_5 cavity (maintained at 80 °C) and TDI heated at 80 °C (grey crosses), 95 °C (blue circles) and 200 °C (orange squares). Solid lines in the same colour represent corresponding linear regressions. The slopes ± 2σ are indicated in the legend and correspond to the NO_3 wall loss rate.

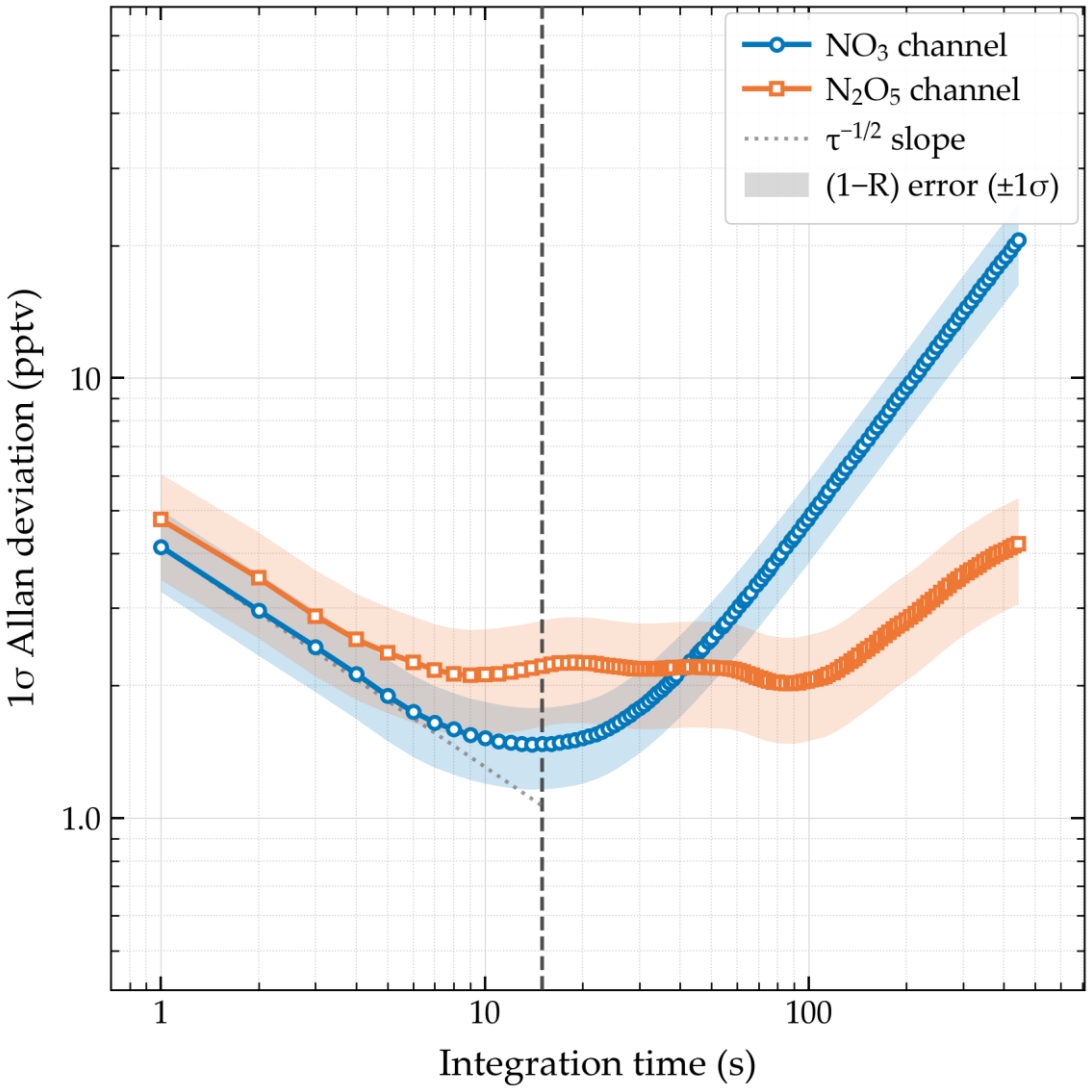


Figure 6. Overlapping Allan deviation (1σ) in dependence of the NO_3 channel's (blue circles) and N_2O_5 channel's (orange squares) integration time. The grey dashed line marks the $^{1}/_{\sqrt{\tau}}$ slope. Ther vertical black dashed line marks the optimal integration time of 15 s. The effect of potential variabilities in mirror reflectivity is represented by shaded areas.

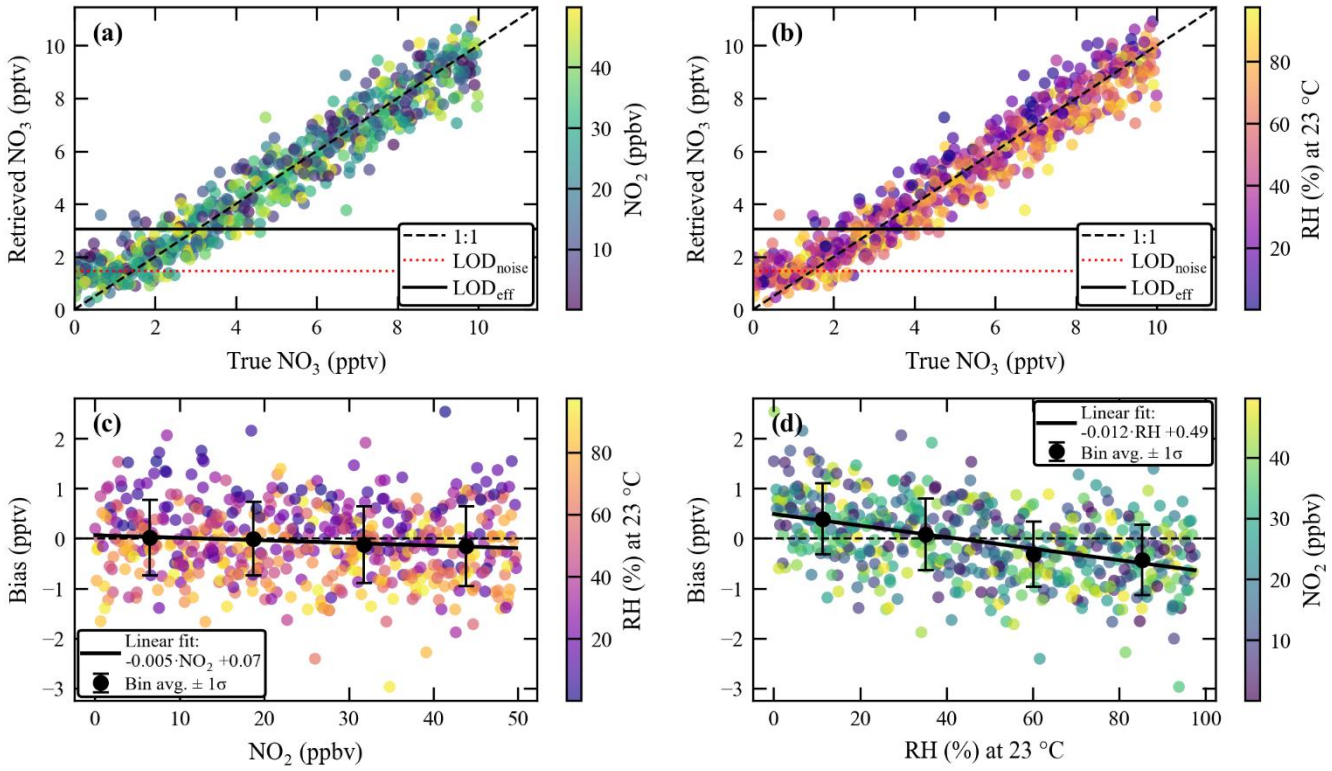


Figure 7. Retrieval performance of the NO_3 fitting routine as a function of interfering NO_2 and water vapor, based on Monte Carlo simulations of synthetic spectra for the NO_3 channel (10 noise realisation points average, 600 LHS points): (a, b) Retrieved vs. true NO_3 mixing ratio, with points colored by (a) true NO_2 (ppbv) and (b) relative humidity (RH, % at 23°C). The dashed line indicates the 1:1 relationship; the dotted red line marks LOD_{noise} derived from the Allan deviation, and the solid black line marks the effective detection limit LOD_{eff}, which additionally incorporates the standard deviation (2σ) of the retrieval bias across all simulated spectra. (c, d) Retrieval bias (retrieved − true NO_3) for points $NO_3 > LOD_{noise}$ plotted against (c) NO_2 and (d) RH, colored by the complementary variable in each case. Black circles show bin-averaged values (± 1σ). Black lines show weighted linear fits to the bin-averaged points.

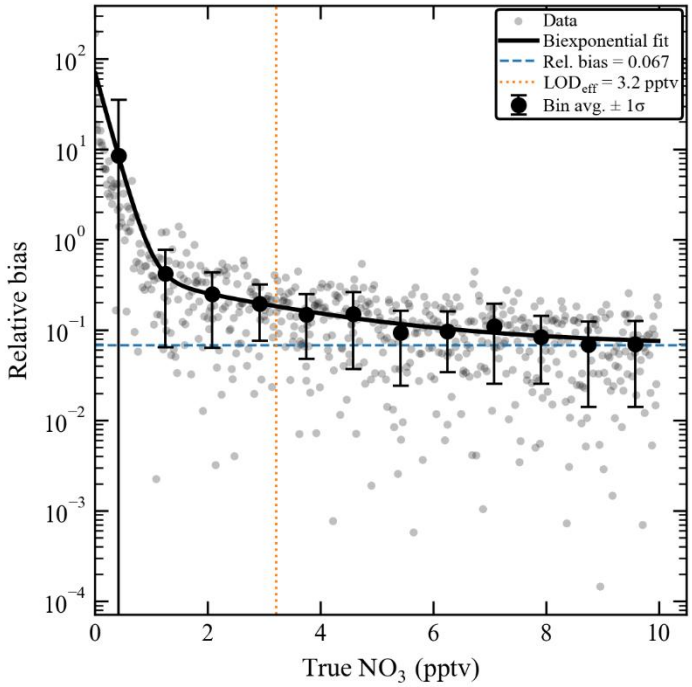


Figure 8. Relative bias in retrieved NO_3 (|retrieved − true| / true) versus true NO_3 concentration from Monte Carlo simulations for the NO_3 channel. Gray points: individual retrievals; black circles: quantile-binned means ± 1σ. Solid line: biexponential fit with parameters (a_1, a_2, b_1, b_2, c), relative bias = a_1 x exp(−b_1 x NO_3) + a_2 x exp(−b_2 x NO_3) + c, capturing the noise-dominated divergence at low NO_3 and the systematic interference floor (c = 0.067, blue dashed line) at higher NO_3. Orange dotted line: effective LOD.

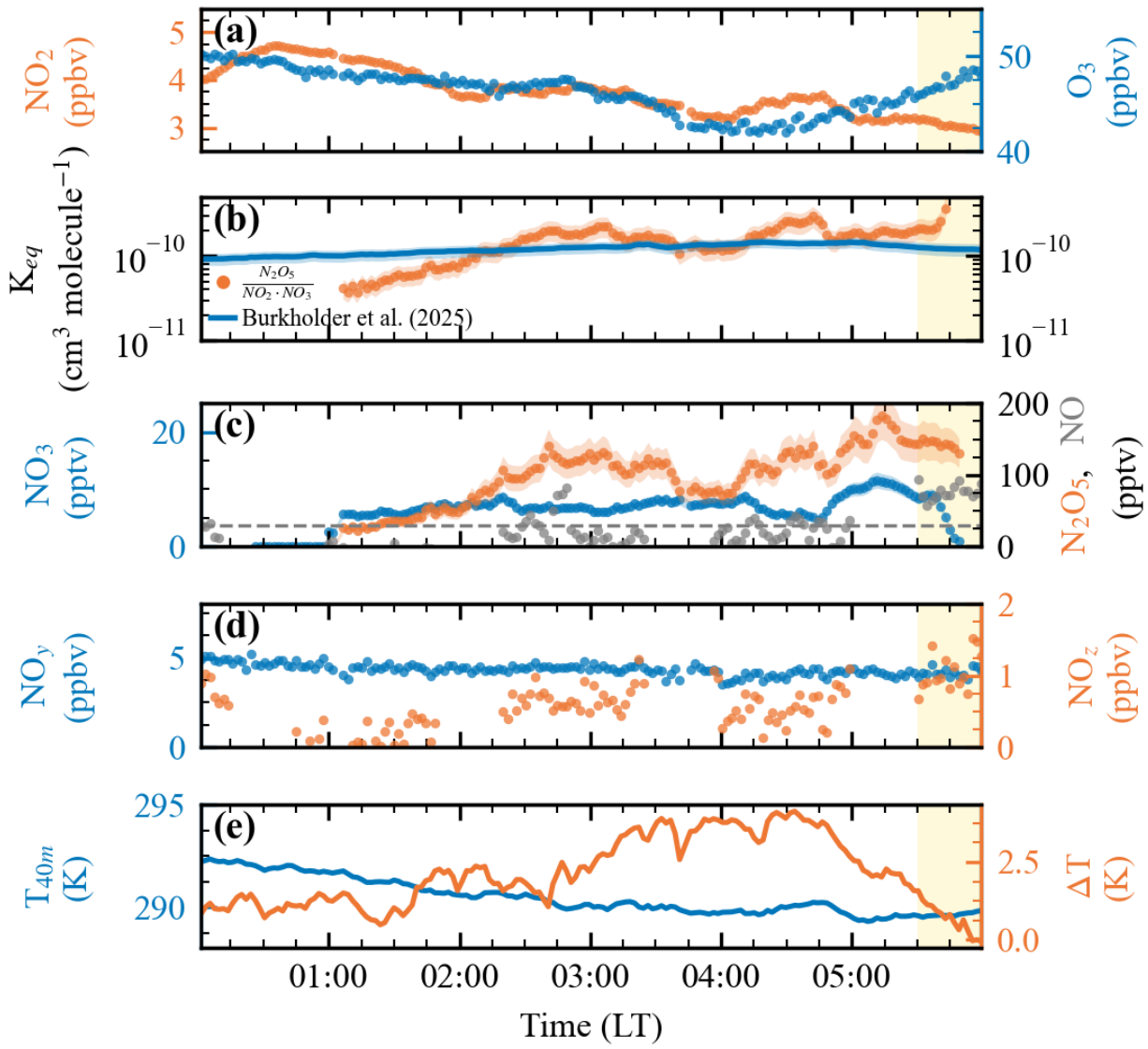


Figure 9. Nocturnal time series during the ACROSS campaign (16–17 July 2022, 00:00–06:00 LT); yellow shading indicates sunrise (05:30 LT). (a) NO_2 (orange, left axis) and O_3 (blue, right axis). (b) Measured NO_3–N_2O_5–NO_2 relationship $[N_2O_5]/([NO_2][NO_3])$ (orange), compared with the evaluated, temperature-dependent equilibrium constant from Burkholder et al. (2025) (blue line, shading = uncertainty). (c) NO_3 (blue, left axis) and N_2O_5 (orange, right axis) mixing ratios with the total measurement uncertainty (shading), alongside NO (gray, right axis, provided py IMT Nord Europe); the dashed line marks the NO detection limit (30 pptv). (d) NO_y (blue, left axis) and NO_z (orange, right axis). (e) Ambient temperature at 40 m (blue, left axis) and the temperature difference ΔT between 5 m and 41 m (orange, right axis) from CNRM (Météo-France).